Spectral and Spatial Modulation of Optical Pump Beam for Mirrorless Optical Parametric Oscillation

A Thesis

submitted to

Indian Institute of Science Education and Research Pune

in Partial fulfilment of the requirements for the

BS-MS Dual Degree Programme

by

Subhasis Behera

Indian Institute of Science Education and Research Pune
Dr. Homi Bhabha Road,
Pashan, Pune 411008, INDIA.

March 2025

Supervisor: **Dr. Ashok K Mohapatra**

CERTIFICATE

This is to certify that this dissertation entitled "**Spectral and Spatial Modulation of Optical Pump Beam for Mirrorless Optical Parametric Oscillation**" towards the partial fulfilment of the BS-MS dual degree programme at the Indian Institute of Science Education and Research, Pune represents study/work carried out by **Subhasis Behera** at National Institute of Science Education and Research, Bhubaneswar under the supervision of **Dr. Ashok K Mohapatra**, Associate Professor, School of Physical Sciences, during the academic year 2024-2025.

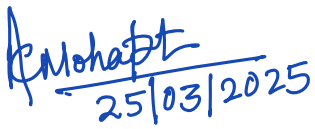

Dr. Ashok K Mohapatra

Committee:

Dr. Ashok K Mohapatra

Dr. Shouvik Datta

This thesis is dedicated to my beloved Parents, **Mr. Paramananda Behera** and **Mrs. Madhumita Dalai.**

DECLARATION

I hereby declare that the matter embodied in the report entitled "**Spectral and Spatial Modulation of Optical Pump Beam for Mirrorless Optical Parametric Oscillation**" are the results of the work carried out by me at the School of Physical Sciences, National Institute of Science Education and Research, Bhubaneswar, under the supervision of Dr. Ashok K Mohapatra, and the same has not been submitted elsewhere for any other degree. Wherever others contribute, every effort is made to indicate this clearly, with due reference to the literature and acknowledgment of collaborative research and discussions.

25/03/2025

Subhasis Behera

ACKNOWLEDGEMENTS

I am extremely grateful to my supervisor Prof. Ashok K. Mohapatra, who has helped me appreciate and enjoy the process of doing science better with his constant support and encouragement. I am truly fortunate to have had the opportunity to learn from such an exceptional guide. I would like to express my sincere gratitude to Dr. Shouvik Datta for his invaluable support as a TAC member. I truly appreciate his willingness to step in on short notice understanding my situation and his advice during the thesis period. My project would have been incomplete without the help of Dr. Surya Narayan Sahoo, who had helped me throughout and was a mentor to me for the project, I am grateful for all the insightful conversations we had and the constant support he has given me. His enthusiasm for science is inspiring, and I will cherish and continue to seek his mentor-ship throughout my journey in science and research. I am indebted to the wonderful members of the Quantum Optics lab Dr. Sujit Garain, Soumya Ranjan Mishra, Soumik Nandi, Tousif Alam, Nandini Mondal, Purvesh Garge, Nikhil Anand, Swarup Kumar Giri, and Hudha P.M. for making it fun and joyous to work in the lab. Their constant support, affection, and invaluable discussions on academia and life have played a key role in bringing more balance to mine. I would like to acknowledge my experiment partner, Daniya C, for her collaboration in the experiment and for motivating me to do better science.

I am forever in gratitude to my parents, Mr. Paramananda Behera and Mrs. Madhumita Dalai, for their unwavering support and encouragement throughout this journey and undoubtedly in the years to come. Their love and positive attitude fuel me to face every situation courageously and push me to be a better person at work and in life. I am also deeply grateful to my best friend, Gayatree Swain, for her constant support and love throughout my academic journey.

ABSTRACT

The advent of lasers in the 1960s as coherent light sources revolutionized nonlinear optics, enabling the exploration of phenomena driven by strong electromagnetic fields. Since then, a wide range of discoveries, such as sum frequency generation, optical parametric oscillation, and four-wave mixing (FWM) etc, have been extensively studied. This thesis focuses on Mirrorless Optical Parametric Oscillation (MOPO), a cavity-free process with high tunability, achieved through FWM, where phase matching is inherently satisfied by counter-propagating pump beams. By investigating the spectral and spatial modulation of pump beams, this work aims to advance the understanding and practical applications of MOPO in nonlinear optics. This process has been demonstrated in both $\chi^{(2)}$ and $\chi^{(3)}$ nonlinear media, leading to the generation and amplification of optical fields from noise due to the interaction of counter-propagating input fields in the nonlinear medium. The work presented in this thesis investigates the spectral and spatial modulation of optical pump beams used for MOPO. This thesis provides a basic theoretical and experimental overview, including the wave analysis of light, key nonlinear optical effects, and the derivation of nonlinear wave equations. It also addresses essential concepts in atomic physics, the application of acousto-optic modulators, and the 4-f imaging technique. The study further investigates the principles and properties of MOPO and explores experimental methods for generating multitone and time-shared pump beams using acousto-optic modulators. By focusing on spectral and spatial modulation, this research advances the understanding and practical applications of MOPO in nonlinear optics.

Contents

List of Figures

List of Tables

Chapter 1

Introduction

The field of nonlinear optics has been extensively studied since the invention of lasers back in the 1960s. When a strong electromagnetic field propagates through a medium, it induces nonlinear polarization within the medium, which leads to nonlinear optical phenomena. While nonlinear optics has many aspects, optical parametric oscillation (OPO) is one of the most efficient processes for generating coherent optical radiation at tunable wavelengths. OPO process relies on an optical cavity formed by mirrors to provide feedback and sustain oscillation. However, the emergence of mirrorless optical parametric oscillation (MOPO) sets a new milestone, offering a cavity-free alternative that simplifies the experimental setup a lot while retaining the ability to produce coherent, tunable light sources. In this thesis, we will discuss the spectral and spatial modulation of a pump beam used for the MOPO. In our case, MOPO results from the four-wave mixing (FWM) mechanism, which is a third-order nonlinear optical process.

OPO basically involves the nonlinear interaction of light fields within a nonlinear medium. The pump beam interacts with the nonlinear medium to generate signal and idler waves. In conventional OPO, the optical cavity, inside which the nonlinear medium is placed, ensures the phase-matching and amplification by the feedback mechanism. In addition, the frequency of the output is related to the alignment of the signal and idler modes with respect to one another, creating the need for considerable stabilization of the optical cavities. MOPO circumvents this issue by utilizing the intrinsic feedback mechanism of the nonlinear medium itself, eliminating the need for an

external cavity. This approach was first proposed by Harris in 1966 [2], who suggested backward wave oscillation in the infrared regime with two counter-propagating beams to satisfy the phase-matching condition automatically. Since then, MOPO has been established in second-order ($\chi^{(2)}$) [3] and third-order ($\chi^{(3)}$) nonlinear media [12, 13]. The latter employs FWM to generate counter-propagating Stokes and anti-Stokes fields spontaneously from noise. Its inherent simplicity and flexibility make MOPO an attractive candidate for a variety of applications ranging from quantum optics to spectroscopy, yet its full potential has yet to be explored, particularly with respect to the pump beam's spectral and spatial properties. The motivation for this work is based on the idea that the characteristics of the pump beam -its frequency and spatial profile- play a crucial role in determining the efficiency and bandwidth of the generated fields in MOPO. In previous studies of MOPO, like [12, 13], a single-frequency pump and control beam have been used, resulting in Stokes and anti-Stokes fields with well-defined frequencies determined by energy conservation and phase-matching conditions. However, many applications often require either broader bandwidth or multitone outputs. This raises compelling questions: What happens if the pump beam comprises multiple frequency components (multitone) or is frequency modulated over time (time-shared)? How do these modifications affect the spectral and spatial properties of the generated Stokes and anti-Stokes fields? Addressing these questions requires not only a theoretical framework to model the nonlinear interactions but also experimental techniques to generate and characterize such pump beams. At the heart of this study is the use of an acousto-optic modulator (AOM) to manipulate the spectral and spatial properties of the pump beam. AOMs use the acousto-optic effect, where an acoustic wave induces a periodic variation in the crystal's refractive index, which acts as a traveling grating for incident light. This allows precise control over the beam's frequency and direction, making it an excellent tool

for creating multitone and time-shared frequency profiles. Rubidium (Rb) atomic vapor is used as a nonlinear medium, which is a centrosymmetric medium, which means even order nonlinear susceptibilities are absent, and it is predominantly $\chi^{(3)}$ medium. Rb is chosen for its well-characterized atomic transitions, accessible via diode lasers, and its suitability for FWM process due to its third-order nonlinear susceptibility.

The experimental setup builds on concepts from wave optics, nonlinear optics, and atomic physics, as outlined in Chapter 2 of this thesis. Chapter 3 delves into the specifics of FWM-based MOPO, deriving the nonlinear wave equations for generated fields and posing the research questions that drive this study. Chapter 4 provides the experimental details to generate and analyze multitone and time-shared pump beams, presenting observations that set the stage for further exploration of their effects on MOPO.

Chapter 2

Basic Theoretical and Experimental Tools

2.1 Wave Analysis of Light

In the current section we will discuss about the wave nature of laser beams. We will assume that the apertures (for example, mirror apertures) are so small compared to the transverse extent (spot size) of the beams so that we can neglect the diffraction effects.

2.1.1 Approximate Solution to the Wave Equation

The Spatial part of the field satisfies the **Helmholtz Equation**,

$$\nabla^2 U + k^2 U = 0 \tag{2.1}$$

where $k = \frac{\omega}{c}$ is the magnitude of the Wavevector.

A simple solution to Eq.2.1 is the plane wave solution. The plane wave which is propagating along the $z-$ direction can be written as

$$U(\mathbf{r}) = A \exp\{(-jkz)\} \tag{2.2}$$

A is a complex constant. The plane wave has infinite transverse extent and constant intensity everywhere in space that means it carries infinite amount of energy. So, it is an idealization. We want to construct a beam which has a finite transverse extent and mainly propagates along $z-$ direction (propagation is choosen to be along $z-$

axis). One such good candidate is Paraxial wave. Paraxial waves are those whose wavefront normals are Paraxial rays. We discussed about the Paraxial rays in the earlier section. So, in order to study the Paraxial waves we now allow the complex amplitude (envelope) of the plane wave to vary as a function of position. So our ansatz is

$$U(x, y, z) = \psi(x, y, z) \exp\{(-jkz)\} \tag{2.3}$$

where ψ is a slowly varying function of z (within a distance of wavelength the function doesn't vary much) so that the wave maintains its underlying plane wave nature. Plugging 2.3 into the Helmholtz equation (Eq.2.1), we get

$$\frac{\partial^2\psi}{\partial x^2} + \frac{\partial^2\psi}{\partial y^2} + \frac{\partial^2\psi}{\partial z^2} - 2jk\frac{\partial\psi}{\partial z} = 0 \tag{2.4}$$

Since ψ is a slowly varying function of z, $\frac{\partial^2\psi}{\partial z^2}$ can be neglected in comparision with $k\frac{\partial\psi}{\partial z}$,

$$\boxed{\frac{\partial^2\psi}{\partial x^2} + \frac{\partial^2\psi}{\partial y^2} - 2jk\frac{\partial\psi}{\partial z} = 0} \tag{2.5}$$

The solution of Eq.2.5 is of the form

$$\psi = \exp\left[-j\left(P + \frac{k}{2q}r^2\right)\right] \tag{2.6}$$

where,

$$r^2 = x^2 + y^2 \tag{2.7}$$

The parameter $P(z)$ represents a complex phase shift associated with the propagation of the beam and the parameter $q(z)$ is the complex beam parameter which describes the variation of the intensity profile from the optic axis, curvature of the wavefront etc which we will discuss in this section. Inserting Eq.2.6 into Eq.2.5 we get,

$$-\frac{2jk}{q} - \frac{k^2}{q^2}r^2 - 2k\frac{dP}{dz} + \frac{k^2r^2}{q^2}\frac{dq}{dz} = 0 \tag{2.8}$$

Comparing coefficient of r^2 we get,

$$-\frac{k^2}{q^2}+\frac{k^2}{q^2}\frac{dq}{dz}=0 \tag{2.9}$$

Hence,

$$\boxed{\frac{dq}{dz}=1} \tag{2.10}$$

Comparing constant terms,

$$-\frac{2jk}{q}-2k\frac{dP}{dz}=0 \tag{2.11}$$

Or,

$$\boxed{\frac{dP}{dz}=-\frac{j}{q}} \tag{2.12}$$

Keeping in mind Eq.2.10 we define the complex beam parameter as

$$q=z+jz_0 \tag{2.13}$$

z_0 is called the Rayleigh range which is a measure of focal region of the beam. For convenience we introduce the parameters R and w as,

$$\frac{1}{q}=\frac{1}{R(z)}-j\frac{\lambda}{\pi w(z)^2} \tag{2.14}$$

The physical significance of these two parameters can be inferred by putting Eq.2.14 into Eq.2.6. $R(z)$ is the wavefront radius of curvature which intersects the axis at z whereas $w(z)$ is the radius of the beam. At any distance z on the axis of the beam, the transverse profile of the beam is Gaussian and w is the distance at which the amplitude is $\frac{1}{e^2}$ times that on the axis. Therefore, it is called the beam radius. Plugging 2.13 into 2.14 and separating the real and imaginary part we can readily get the expression for $R(z)$ and $w(z)$.

$$R(z)=z\left[1+\left(\frac{z_0}{z}\right)^2\right] \tag{2.15}$$

$$w(z) = w_0 \left[1 + \left(\frac{z}{z_0}\right)^2\right]^{\frac{1}{2}} \tag{2.16}$$

$$w_0 = \left(\frac{\lambda z_0}{\pi}\right)^{\frac{1}{2}} \tag{2.17}$$

Now we would like to focus our attention to the Complex phase shift part. Putting Eq.2.13 into Eq.2.12, we get,

$$\frac{dP}{dz} = -\frac{j}{z + z_0} \tag{2.18}$$

Rationalizing it we get,

$$\frac{dP}{dz} = -\frac{z_0}{z^2 + z_0^2} - j\frac{z}{z^2 + z_0^2} \tag{2.19}$$

Integrating Eq.2.19, we get,

$$P(z) = -j\left[\frac{1}{2}\ln\left(z^2 + z_0^2\right)\right] - \arctan\left(\frac{z}{z_0}\right) \tag{2.20}$$

The real part of P represents the phase shift difference between the ideal plane wave and the Gaussian beam whereas the imaginary part gives rise to an amplitude factor of $\frac{w_0}{w}$ which explains the decrease in intensity on the axis due to the expansion of the beam. This statement will be clearer if we plug Eq.2.14 and Eq.2.20 into Eq.2.6 and then get the Field from Eq.2.3.

$$U(x, y, z) = \frac{w_0}{w} \exp\left[-j\left(kz - \arctan\left(\frac{z}{z_0}\right)\right) - r^2\left(\frac{1}{w^2} + \frac{jk}{2R}\right)\right] \tag{2.21}$$

or,

$$U(x, y, z) = \frac{w_0}{w} \exp\left[-\frac{r^2}{w^2}\right] \exp\left[-jkz + j\arctan\left(\frac{z}{z_0}\right) - jk\frac{r^2}{2R}\right] \tag{2.22}$$

The phase can be written as,

$$\Phi = kz - \arctan\left(\frac{z}{z_0}\right) + k\frac{r^2}{2R} \tag{2.23}$$

This solution is known as *Gaussian Beam* solution.

2.1.2 Higher Order Modes

The solution discussed above is not the only solution to Eq.2.5. Infact, there are a class of solutions which forms a complete and orthogonal set and the solution discussed above is the lowest-order solution.

System with Rectangular Symmetry (Hermite-Gaussian Modes)

For a system with rectangular symmetry, the trial solution in Eq.2.6 multiplied by Hermite polynomials is also the solution of Eq.2.5.

$$\psi = H_m\left(\sqrt{2}\,\frac{x}{w}\right) H_n\left(\sqrt{2}\,\frac{y}{w}\right) \exp\left[-j\left(P + \frac{k}{2q}(x^2+y^2)\right)\right] \tag{2.24}$$

where $H_m(x)$ denotes the Hermite polynomial of order m. The Parameters R and w defined in the previous section (Eq.2.14) is remain the same for all modes, which implies that the Radius of curvature of the wavefront and the waist radius changes the same way for modes of all order. However, the phase is now modified which depends on the mode numbers m and n. (In other words, q parameter remain the same as discussed in the previous section (Eq.2.13, Eq.2.14) but P parameter is now different from Eq.2.20). The P parameter is given by,

$$P(z) = -j\left[\frac{1}{2}\ln\left(z^2 + z_0^2\right)\right] - (m+n+1)\arctan\left(\frac{z}{z_0}\right) \tag{2.25}$$

The total expression for field becomes,

$$U(x,y,z) = \frac{w_0}{w} H_m\left(\sqrt{2}\,\frac{x}{w}\right) H_n\left(\sqrt{2}\,\frac{y}{w}\right) \exp\left[-\frac{x^2+y^2}{w^2}\right] \exp\left[-jkz + j(m+n+1)\arctan\left(\frac{z}{z_0}\right) - jk\frac{x^2+y^2}{2R}\right] \tag{2.26}$$

with the phase given by,

$$\Phi = kz - (m+n+1)\arctan\left(\frac{z}{z_0}\right) + k\,\frac{x^2+y^2}{2R} \tag{2.27}$$

It is clear from these equations that, when we put $m = 0, n = 0$, these equations reduces to the equations derived in the previous section. i.e. the Gaussian beam is the lowest order mode.

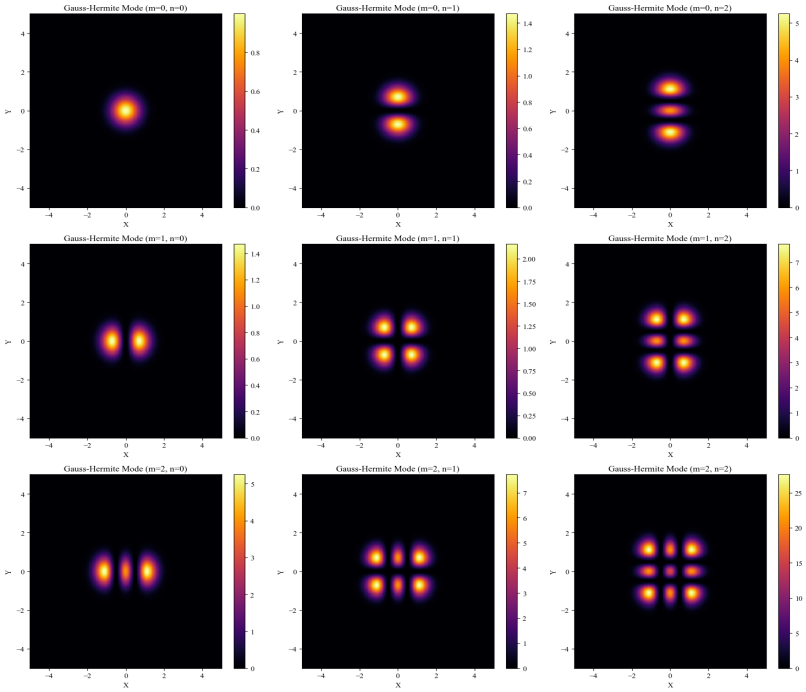

Figure 2.1: First few Hermite-Gaussian Modes

System with Cylindrical Symmetry (Laguerre-Gaussian Modes)

For a system with cylindrical symmetry, the solution for Eq.2.5 is of the form

$$\psi = \left(\sqrt{2}\ \frac{r}{w}\right)^{l}\ L_p^l\left(2\ \frac{r^2}{w^2}\right)\exp\left[-j\left(P + \frac{k}{2q}r^2 + l\phi\right)\right] \tag{2.28}$$

where L_p^l is a generalized Laguerre polynomial. p and l represents the radial and angular mode numbers. Like the Hermite-Gaussian mode case, the beam parameters R and w are the same for all cylindrical modes. However, the phase is modified depending upon the mode numbers p and l. The P parameter is given by,

$$P(z) = -j\left[\frac{1}{2}\ln\left(z^2 + z_0^2\right)\right] - (2p + l + 1)\arctan\left(\frac{z}{z_0}\right) \tag{2.29}$$

The total expression for field becomes,

$$U(x,y,z) = \frac{w_0}{w}\ \left(\sqrt{2}\ \frac{r}{w}\right)^{l}\ L_p^l\left(2\ \frac{r^2}{w^2}\right)\ \exp\left[-\frac{r^2}{w^2}\right] \exp\left[-jkz + j(2p + l + 1)\arctan\left(\frac{z}{z_0}\right) - jk\frac{r^2}{2R} + jl\phi\right] \tag{2.30}$$

with the phase given by,

$$\Phi = kz - (2p + l + 1)\arctan\left(\frac{z}{z_0}\right) + k\ \frac{r^2}{2R} - l\phi \tag{2.31}$$

Here also $p = 0$ and $l = 0$ gives rise to the Gaussian mode.

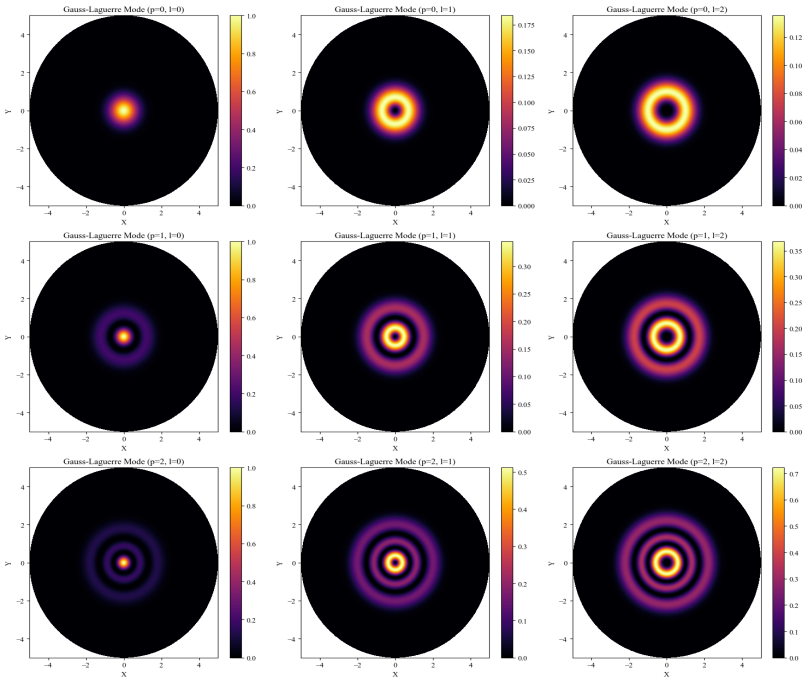

Figure 2.2: First few Laguerre-Gaussian Modes

2.2 Basics of Nonlinear Optics

In the linear optics regime, where the intensity of the field is low, the induced polarization $P(t)$ in a dielectric medium depends linearly on the electric field strength $E(t)$,

$$P(t) = \epsilon_0 \chi^{(1)} E(t) \tag{2.32}$$

where the constant of proportionality $\chi^{(1)}$ is known as the linear susceptibility and ϵ_0 is the permitivity of the free space. However, the above relation is no longer valid, the moment we go to the high intensity field. In such cases, the optical response of the medium can be described by generalizing Eq.2.32, by expressing the polarization $P(t)$ as a power series in the field strength $E(t)$ as

$$P(t) = \epsilon_0 \left[\chi^{(1)} E(t) + \chi^{(2)} E^2(t) + \chi^{(3)} E^3(t) + ...\right] \tag{2.33}$$

$$= P^{(1)}(t) + P^{(2)}(t) + P^{(3)}(t) + ... \tag{2.34}$$

Here $\chi^{(2)}$ and $\chi^{(3)}$ are known as the second and third order nonlinear optical susceptibilities whereas $P^{(2)}(t)$ and $P^{(3)}(t)$ represents the second and third order nonlinear polarization respectively. For the case of centrosymmetric media, i.e. the media possessing inversion symmetry, the second order nonlinear susceptibility, $\chi^{(2)}$ vanishes. Infact, all other higher-order even susceptibilities vanishes as well. Glass, liquid, atomic vapors are some examples of centrosymmetric media. Our working system, the Rb atomic vapor is a centrosymmetric medium. So, we are particularly interested in studying the $\chi^{(3)}$ effect. Some of the $\chi^{(3)}$ effects are discussed briefly in the following sections.

2.2.1 Self-Phase Modulation

Self-phase modulation (SPM) is the change in the optical phase of the light beam caused by its own Intensity. The schematics of the process in a two-level system is depicted in Fig.2.3. It involves the absorption of two photons and stimulated emission of two photons from the input field. The induced Polarization due to SPM is given by,

$$P^{(3)}_{SPM}(\omega_s) = 3\epsilon_0 \chi^{(3)}_{SPM}(\omega_s - \omega_s + \omega_s)|E_s|^2 E_s \tag{2.35}$$

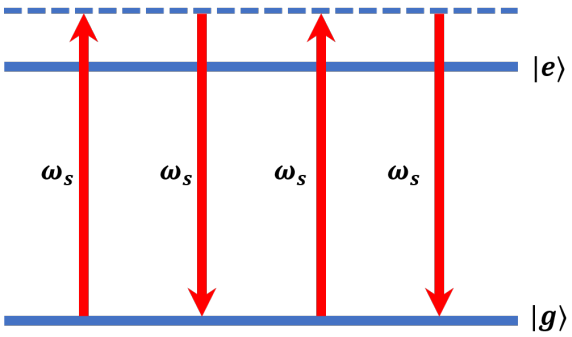

Figure 2.3: Schematics of Self Phase Modulation process in a two-level system

SPM leads to a nonlinear refractive index, $n_2 I_s$, which is intensity dependent.

Here $n_2 = \frac{3}{2n_0^2\epsilon_0 c}\chi^{(3)}_{SPM}$ and I_s is the input light intensity.

2.2.2 Cross-Phase Modulation

XPM leads to nonlinear gain or absorption and the intensity dependent refractive index of the beam due to the interaction of the beam with another pump beam in a nonlinear medium. The schematics of the process in a two-level system is depicted in Fig.2.4. The induced polarization experienced by the weak field, $E_s \exp\{i(k_s z - \omega_s t)\}$ due to the cross phase modulation by a pump field,$E_p \exp\{i(k_p z - \omega_p t)\}$is given by,

$$P^{(3)}_{XPM}(\omega_s) = 3\epsilon_0 \chi^{(3)}_{XPM}(\omega_p - \omega_p + \omega_s)|E_p|^2 E_s \tag{2.36}$$

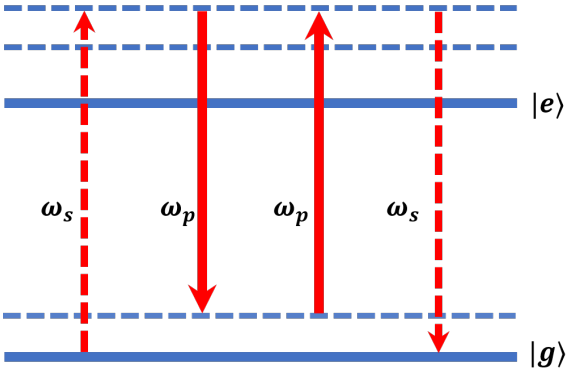

Figure 2.4: Schematics of Cross Phase Modulation process in a two-level system

2.2.3 Four-Wave Mixing

Four-wave mixing (FWM) is a third order optical nonlinear process which involves interaction of four waves in a nonlinear medium. Fig.2.5 depicts the FWM process in a two-level system. It can be stimulated or spontaneous. In the stimulated FWM process, three input beams interact to produce the fourth one, whereas the spontaneous FWM involves the spontaneous generation of two weak fields from the two input pump fields.

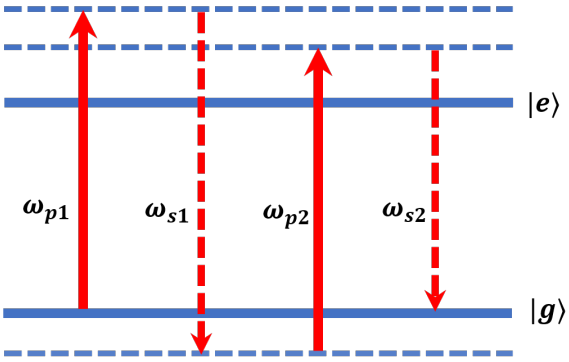

Figure 2.5: Schematics of Four-Wave Mixing in a two-level system

It is a parametric process, which means the initial and final state of the atom is the same. Therefore, the energy and momentum conservation are satisfied by the photon only. Then induced polarization due to the FWM process (Referring to Fig.2.5) is given by,

$$P^{(3)}_{FWM}(\omega_{s2}) = 3\epsilon_0\chi^{(3)}_{FWM}(\omega_{p1} - \omega_{s1} + \omega_{p2})E_{p1}E_{p2}E^*_{s1}\exp\{i(k_{p1} + k_{p2} - k_{s1})z\} \quad (2.37)$$

The conservation of energy implies $\omega_{p1} + \omega_{p2} = \omega_{s1} + \omega_{s2}$ and the phase matching condition, which is basically the conservation of momentum, implies the following relation, $\vec{k_{p1}} + \vec{k_{p2}} = \vec{k_{s1}} + \vec{k_{s2}}$.

2.2.4 Nonlinear Wave Equation

The Maxwell equation inside matter where there is no free charge or free current, can be written as,

$$\nabla \cdot \mathbf{D} = 0 \quad (2.38)$$

$$\nabla \cdot \mathbf{B} = 0 \quad (2.39)$$

$$\nabla \times \mathbf{E} = -\frac{\partial \mathbf{B}}{\partial t} \quad (2.40)$$

$$\nabla \times \mathbf{H} = \frac{\partial \mathbf{D}}{\partial t} \quad (2.41)$$

We also assume that the material is nonmagnetic, so that

$$\mathbf{B} = \mu_0 \mathbf{H} \tag{2.42}$$

However, we allow the material to be nonlinear in the sense that the fields $\mathbf{D}$ and $\mathbf{E}$ are related by

$$\mathbf{D} = \epsilon_0 \mathbf{E} + \mathbf{P} \tag{2.43}$$

where in general the polarization vector $\mathbf{P}$ depends nonlinearly upon the local value of the electric field strength $\mathbf{E}$.

Taking the curl of Eq.2.40 and using 2.41, 2.42 & 2.43, we get

$$\nabla \times \nabla \times \mathbf{E} + \frac{1}{c^2}\frac{\partial^2}{\partial t^2}\mathbf{E} = -\frac{1}{\epsilon_0 c^2}\frac{\partial^2}{\partial t^2}\mathbf{P} \tag{2.44}$$

Using the Identity,

$$\nabla \times \nabla \times \mathbf{E} = \nabla(\nabla \cdot \mathbf{E}) - \nabla^2 \mathbf{E} \tag{2.45}$$

In the linear optics regime, $\nabla \cdot \mathbf{D} = 0$ implies that $\nabla \cdot \mathbf{E} = 0$. However, in nonlinear optics this is not true because of the more general relation Eq.2.43. However, the first term in the RHS of Eq.2.45 can be shown to be very small whenever the slowly varying amplitude approximation is valid. So, we can neglect that term. Now, Substituting these in Eq.2.44, we get,

$$\nabla^2 \mathbf{E} - \frac{1}{c^2}\frac{\partial^2}{\partial t^2}\mathbf{E} = \mu_0 \frac{\partial^2}{\partial t^2}\mathbf{P} \tag{2.46}$$

Now decomposing $\mathbf{P}$ into its linear and nonlinear part,

$$\mathbf{P} = \epsilon_0 \chi^{(1)} \mathbf{E} + \boldsymbol{P_{NL}} \tag{2.47}$$

Substituting Eq.2.47 into Eq.2.46, we get the form for the nonlinear wave equation as,

$$\boxed{\nabla^2 \mathbf{E} - \frac{1}{c^2}(1 + \chi^{(1)})\frac{\partial^2}{\partial t^2}\mathbf{E} = \mu_0 \frac{\partial^2}{\partial t^2}\boldsymbol{P_{NL}}} \tag{2.48}$$

2.3 Basics of Atomic Physics

2.3.1 Energy levels in atoms

Our work is centered around the Rb atom, which has only one valence electron. So, we focus our attention on the case of the hydrogen-like atom. We solve the Schrodinger equation for the system.

$$\frac{\hbar^2}{2\mu}\left[\frac{\partial^2\Psi(x,y,z,t)}{\partial x^2}+\frac{\partial^2\Psi(x,y,z,t)}{\partial y^2}+\frac{\partial^2\Psi(x,y,z,t)}{\partial z^2}\right]+V(x,y,z)\Psi(x,y,z,t)=i\hbar\frac{\partial\Psi(x,y,z,t)}{\partial t} \tag{2.49}$$

Where μ is the reduced mass of the nucleus and electron system, and $V(x,y,z)$ is the Coulomb potential between the nucleus and the electron, given by

$$V(x,y,z)=-\frac{Ze^2}{4\pi\varepsilon_0\sqrt{x^2+y^2+z^2}} \tag{2.50}$$

The general solution to Eq.2.49 in spherical coordinates is of the form $R_{nl}(r)\Theta_{lm_l}(\theta)\Phi_{m_l}(\phi)$,

$$n=1,2,3,\ldots \tag{2.51}$$

$$l=0,1,2,\ldots,n-1 \tag{2.52}$$

$$m_l=-l,-l+1,\ldots,0,\ldots,l-1,l \tag{2.53}$$

The energy eigenvalues are given by:

$$E_n=-\frac{\mu Z^2e^4}{(4\pi\varepsilon_0)^2 2\hbar^2n^2} \tag{2.54}$$

Orbital Angular Momentum

The z-component of the angular momentum operator satisfies the following eigenvalue equation:

$$\hat{L}_z\left|z\right\rangle=m_l\hbar\left|z\right\rangle \tag{2.55}$$

where $|z\rangle$ is the eigenstate of $\hat{L}_z$ operator. The Orbital angular momentum operator satisfies the following equation,

$$\hat{L^2}\,|l\rangle = l(l+1)\hbar^2\,|l\rangle \tag{2.56}$$

where $|l\rangle$ is the eigenstate of $\hat{L}$ operator.

Spin-Orbit Coupling

The orbital motion, as well as the intrinsic spin of an electron can produce magnetic fields. The interaction of these two magnetic fields is called spin-orbit coupling. It is responsible for the fine structure of atoms.

Total Angular Momentum

The total angular momentum **J** is defined as

$$\mathbf{J} = \mathbf{L} + \mathbf{S} \tag{2.57}$$

Where **L** is the total orbital angular momentum operator, whereas **S** is the spin angular momentum operator. Like the orbital and spin angular momentum, it also follows the same angular momentum algebra.

$$J = \sqrt{j(j+1)}\hbar \tag{2.58}$$

$$j_z = m_j\hbar \tag{2.59}$$

j can take values from $l-s$ to $l+s$ in integer steps and m_j can take values from $-j$ to j in integer steps.

Hyperfine Splitting

Till now, we have considered the nucleus as an object of charge $+Ze$ and mass M_N. But the nucleus also has spin angular momentum **I**. The nuclear spin **I** interacts with

the electron total angular momentum **J** giving rise to the Hyperfine splitting. The total angular momentum **F** of the atom can be written as

$$\mathbf{F} = \mathbf{I} + \mathbf{J} \tag{2.60}$$

2.3.2 Selection Rules

The generalized selection rules for electric dipole transitions in the $LS-$coupling scheme are

1. $\Delta J = 0, \pm 1$ ($J = 0 \longleftrightarrow J' = 0$ forbidden)
2. $\Delta M_J = 0, \pm 1$ ($M_J = 0 \longleftrightarrow M_{J'} = 0$ forbidden if $\Delta J = 0$)
3. Parity Changes
4. $\Delta l = 0, \pm 1$

   In addition to these, the following are obeyed whenever L and S are good quantum numbers.
5. $\Delta L = 0, \pm 1$ ($L = 0 \longleftrightarrow L' = 0$ forbidden)
6. $\Delta S = 0$

2.3.3 Properties of Rubidium

Rubidium is a very good candidate for atomic physics experiments as the diode lasers corresponding to the optical transition frequencies are readily available. It is an alkali metal with atomic number 37 with a single valence electron and hydrogen-like atomic structure. Natural rubidium comprises of two isotopes, a stable isotope ^{85}Rb with 72% abundance, as well as a slightly radioactive isotope ^{87}Rb with 28% abundance. The ^{87}Rb has a half-life of 48.8 billion years.

The schematic energy level diagram for D_1 and D_2 lines ^{85}Rb and ^{87}Rb are shown in Fig.2.6 and Fig.2.7 respectively. The D_1 line corresponds to $5S_{1/2}$ to $5P_{1/2}$ transition whereas D_2 line corresponds to $5S_{1/2}$ to $5P_{3/2}$ transition. The ^{85}Rb has a nuclear spin $I = 5/2$. So, the states $5S_{1/2}$ and $5P_{1/2}$ $(J = 1/2)$ splits into two hyperfine states $F = 2$ and $F = 3$ whereas the state $5P_{3/2}$ splits into 4 hyperfine states $F = 1, 2, 3, 4$. Similarly,the ^{87}Rb has a nuclear spin $I = 3/2$. So, the states $5S_{1/2}$ and $5P_{1/2}$ $(J = 1/2)$ splits into two hyperfine states $F = 1$ and $F = 2$ whereas the state $5P_{3/2}$ splits into 4 hyperfine states $F = 0, 1, 2, 3$.

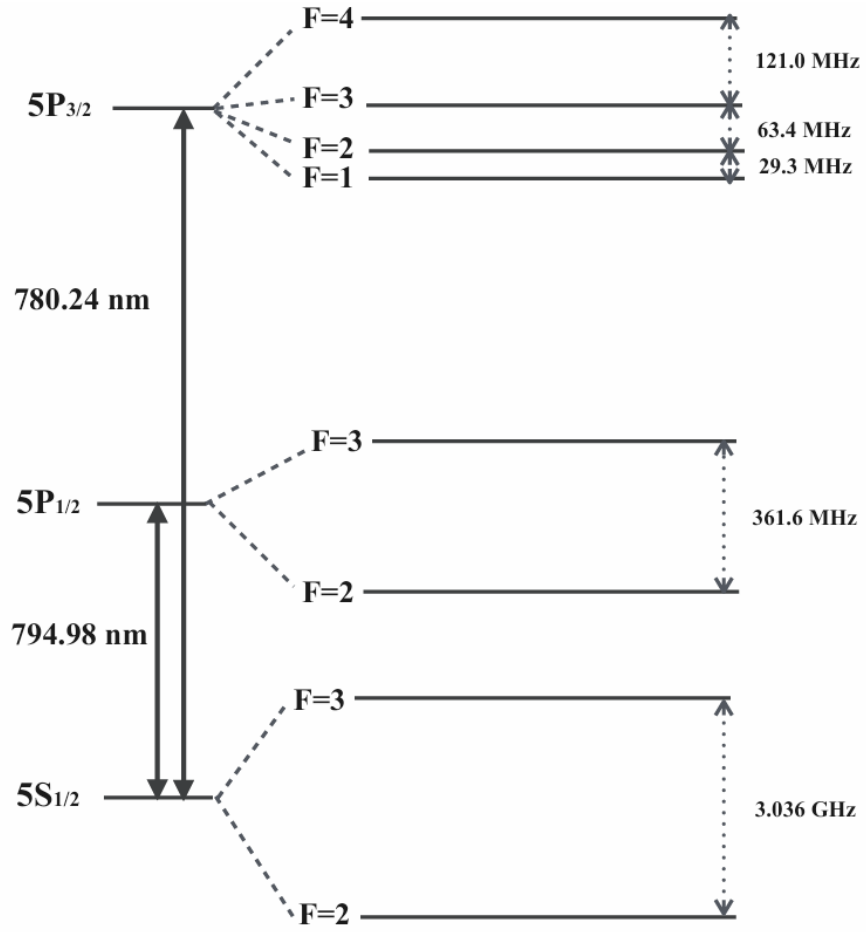

Figure 2.6: Schematic diagram of energy level configuration for D_1 and D_2 lines of ^{85}Rb ([1])

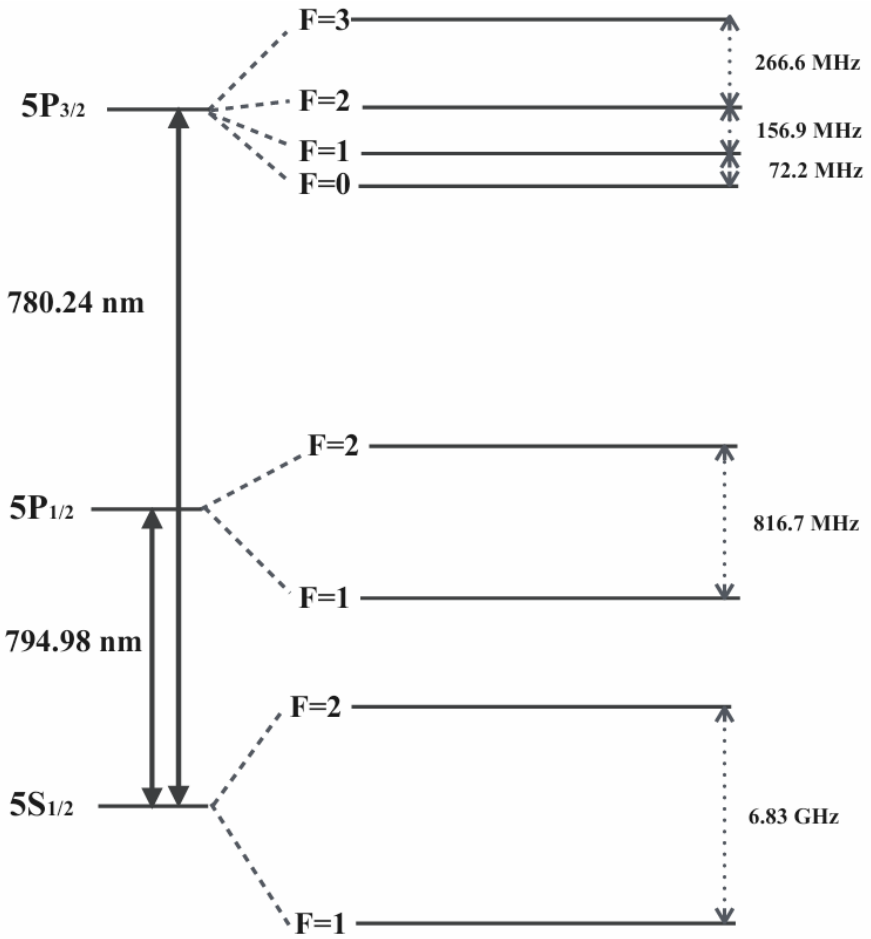

Figure 2.7: Schematic diagram of energy level configuration for D_1 and D_2 lines of ^{87}Rb ([1])

2.4 Acousto-Optic Modulator (AOM)

An Acousto-Optic Modulator (AOM) is a device that uses the acousto-optic effect, i.e. the modification of the refractive index of the material due to the oscillating mechanical strain of the sound wave, to diffract and shift the frequency of the light. It consists of a transparent crystal attached to a piezoelectric transducer in one end. This transducer receives strong oscillating RF signal from the driver. It excites a sound wave of the frequency set by the driver inside the crystal. The other end of the crystal is attached to the absorber which absorbs the sound wave transmitted

through the crystal. The compression and rarefaction of the sound wave leads to a periodic variation of the density and therefore the refractive index of the crystal. It acts as a diffraction grating for the incident light wave and infact the geometry of the entire device ensures a travelling grating. Therefore, light incident on the crystal diffracted from the acoustic wavefront and light diffracted from the successive wavefronts interferes constructively. The Bragg condition for constructive interference reads,

$$\sin\theta = \frac{\lambda}{2\Lambda} \tag{2.61}$$

where θ is the angle of incidence, called the Bragg angle, λ is the wavelength of the light and Λ is the acoustic wavelength.

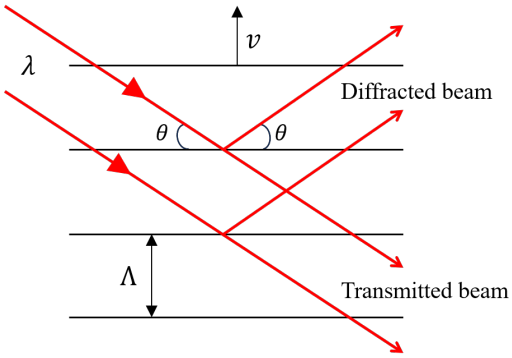

Figure 2.8: Bragg construction for Constructive Interference

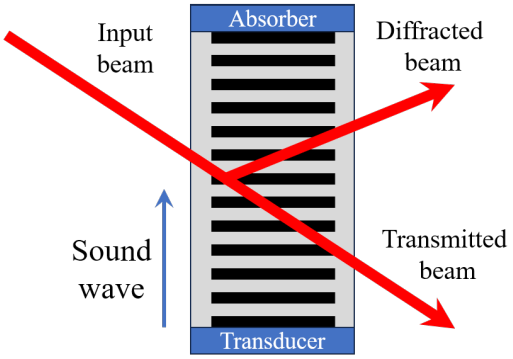

Figure 2.9: Schematics of AOM

2.5 4-f Imaging

Image is basically a one-to-one mapping of the object. 4-f imaging is a setup where the distance between the object plane and the image plane is 4-f, where f is the focal length of the lens. The schematic of the 4-f imaging setup is shown in Fig.2.10.

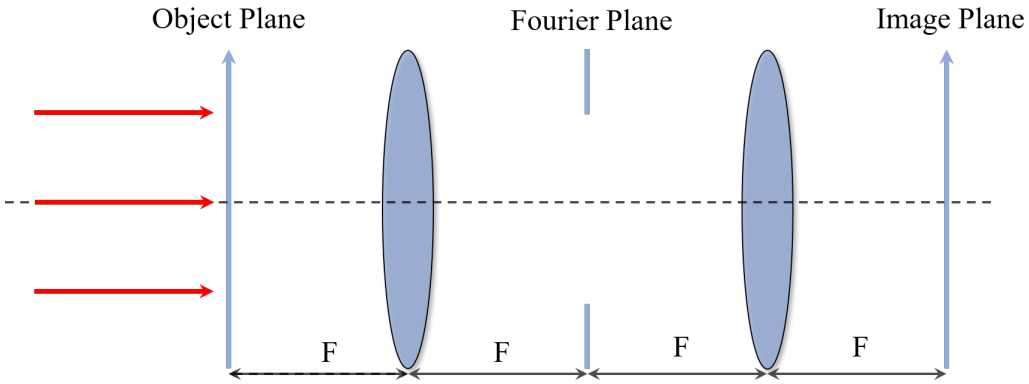

Figure 2.10: 4-f Imaging Setup

Two lenses of focal length f are situated at a distance 2f apart. An object is placed at a distance of f from the first lens; then, the image is formed at a distance of f from the second lens, making the distance between the object plane and image plane 4f. The feature of any imaging system is that it should be diffraction-free. On top of that, a 4-f imaging system provides the image of the object with unit magnification.

Suppose the object is slightly off from the focus of the first lens, then Fig.2.11 and Fig.2.12 illustrates the image distance from the second lens and the total magnification of the image respectively. The focal length of the lens is taken to be 5 cm and we plotted the image distance and magnification for the case where our object is within 2 cm off in either side.

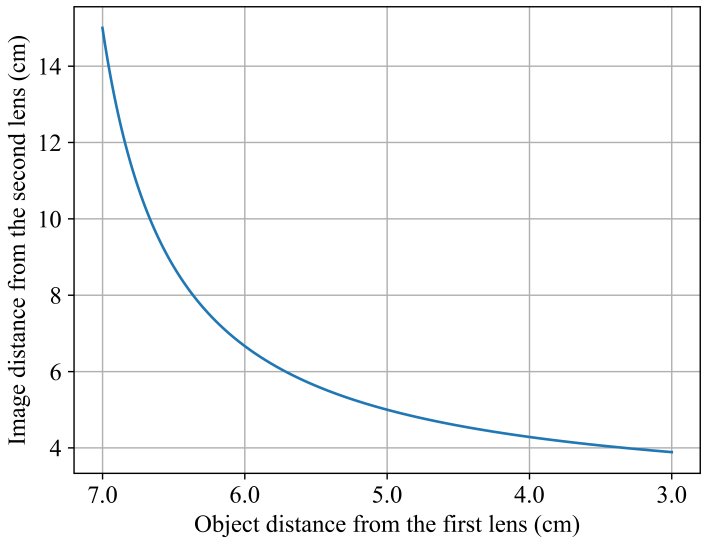

Figure 2.11: Plot showing image distance from the second lens as a function of object distance from the first lens

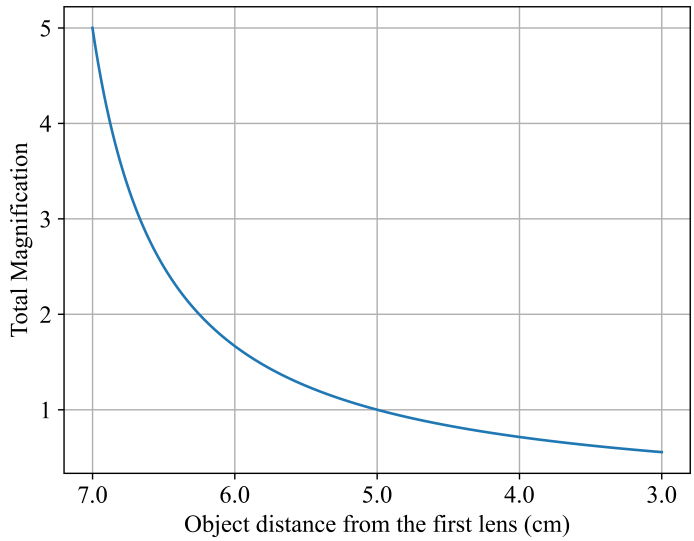

Figure 2.12: Plot showing total magnification as a function of object distance from the first lens

There are certain advantages of 4-f imaging over the 2-f imaging. 2-f imaging system uses single lens to image the object. Suppose the beams are coming parallel then it will focus to a single point. Hence, it is no longer a one-to-one mapping. Such setup only works in the diverging case. But the 4-f imaging is always a one-to-one mapping of the object.

We used a 4-f imaging system to image the focal plane of the Objective lens. Two 5 cm lenses are used in that setup. Since we are focusing the beam through the Objective, the divergence is very high. This is the reason why we used the short focal length lens. To find the focus spot, the test target *Thorlabs R1DS1N* is used. We first put two 5 cm lenses 10 cm apart. Then we put the test target in the object plane and put the camera in the image plane. The distances were finely adjusted by putting the test target as well as the camera in the translation stage. Fig.2.13 shows the heatmap of the test target image obtained in the camera.

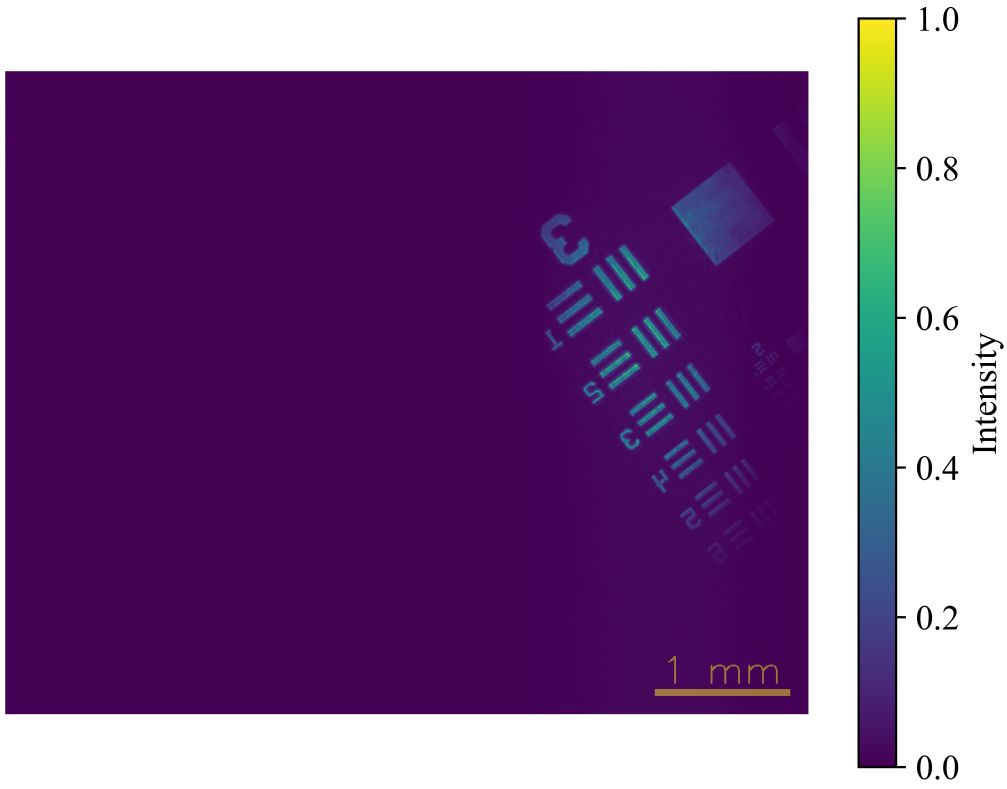

Figure 2.13: Heatmap of the test target image obtained in the camera

Chapter 3

Mirrorless Optical Parametric Oscillation

There are certain advantages of MOPO over traditional OPOs, like the feedback mechanism is internal, which means the feedback is coming from the optical nonlinearity itself and we can study the multitone and time-shared pump beam in MOPO. The phase-matching condition, which is essentially the conservation of momentum, must be satisfied for the process to be efficient. In the case of MOPO, this condition is satisfied by the counter-propagating geometry of the pump and control beams. In $\chi^{(3)}$ medium, MOPO can be achieved by the FWM process [12, 13].

3.1 Principle of FWM-based MOPO

MOPO arises from the nonlinear interaction between counter-propagating pump and control fields, resulting in the parametric generation of counter-propagating Stokes and anti-Stokes fields without requiring an optical cavity. As illustrated in Fig. 3.1, the process involves a three-level atomic system driven by two classical laser fields. The Stokes and anti-Stokes fields are spontaneously generated and amplified through an FWM process, where the feedback is established by the FWM process itself. The Stokes and the anti-Stokes beam travel along the pump and control beam directions, respectively, which is a consequence of phase-matching conditions.

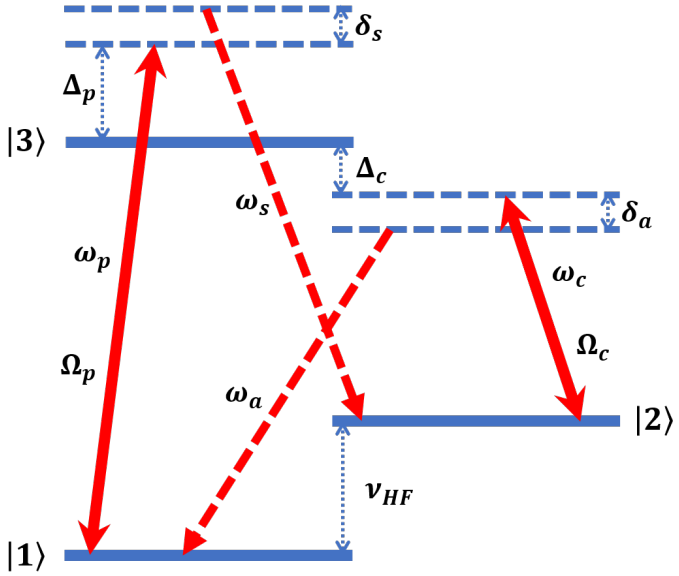

Figure 3.1: Energy level diagram illustrating the MOPO process

The system depicted in Fig.3.1 illustrates a double-Λ configuration, where $|1\rangle$ and $|2\rangle$ represent the hyperfine ground states. One of the virtual excited states is red-detuned, and another is blue-detuned from the state $|3\rangle$. The pump laser beam, characterized by a Rabi frequency Ω_p and optical frequency ω_p, excites atoms from $|1\rangle$ to a state that is blue-detuned by Δ_p relative to $|3\rangle$. Likewise, a control laser beam, with Rabi frequency Ω_c and optical frequency ω_c, is red-detuned by Δ_c from the $|2\rangle \rightarrow |3\rangle$ transition. These pump and control fields propagate in opposite directions within the atomic medium. As a result of non-degenerate FWM, counter-propagating Stokes and anti-Stokes fields generate with optical frequencies ω_s and ω_a, respectively. Their two-photon detunings are given by $\delta_s = \omega_s - \omega_p - \Delta_{LS} + \nu_{HF}$ and $\delta_a = \omega_a - \omega_c + \Delta_{LS} - \nu_{HF}$, where the light shift induced by the pump and control fields is $\Delta_{LS} = \frac{\Omega_p^2}{4\Delta_p} - \frac{\Omega_c^2}{4\Delta_c}$, and ν_{HF} denotes the hyperfine splitting between $|1\rangle$ and $|2\rangle$. Energy conservation in the FWM process imposes the constraint $\omega_p + \omega_c = \omega_s + \omega_a$, ensuring that $\delta_s + \delta_a = 0$.

3.2 Nonlinear Wave Equations for Generated Fields

The nonlinear wave equation as derived in subsection 2.2.4 (2.48) is given by

$$\nabla^2\mathbf{E} - \frac{1}{c^2}(1+\chi^{(1)})\frac{\partial^2}{\partial t^2}\mathbf{E} = \mu_0\frac{\partial^2}{\partial t^2}\boldsymbol{P_{NL}} \tag{3.1}$$

We denote the Electric field for the pump beam as E_p, the control beam as E_c, the Stokes beam as E_s, and the anti-Stokes beam as E_a. We use the convention that the pump beam is propagating along the positive $z-$direction whereas the control beam is propagating along the negative $z-$direction. Hence, it follows from the phase-matching condition that Stokes beam is along positive $z-$direction and the control beam is along negative $z-$direction. We write the electric field for the above fields as,

$$E_p = A_p e^{i(k_p z - \omega_p t)} \tag{3.2}$$

$$E_c = A_c e^{i(-k_c z - \omega_c t)} \tag{3.3}$$

$$E_s = A_s e^{i(k_s z - \omega_s t)} \tag{3.4}$$

$$E_a = A_a e^{i(-k_a z - \omega_a t)} \tag{3.5}$$

Substituting Eq.3.2–Eq.3.5 into Eq.3.1 we get,

$$\nabla_T^2 A_p(z) + 2ik_p\frac{\partial A_p}{\partial z} + \frac{\partial^2 A_p}{\partial z^2} - k_p^2 A_p + \frac{\omega_p^2(1+\chi^{(1)})}{c^2}A_p = -\omega_p^2\mu_0 P^{NL}(\omega_p)e^{-i(k_p z - \omega_p t)} \tag{3.6}$$

$$\nabla_T^2 A_c(z) - 2ik_c\frac{\partial A_c}{\partial z} + \frac{\partial^2 A_c}{\partial z^2} - k_c^2 A_c + \frac{\omega_c^2(1+\chi^{(1)})}{c^2}A_c = -\omega_c^2\mu_0 P^{NL}(\omega_c)e^{-i(-k_c z - \omega_c t)} \tag{3.7}$$

$$\nabla_T^2 A_s(z) + 2ik_s\frac{\partial A_s}{\partial z} + \frac{\partial^2 A_s}{\partial z^2} - k_s^2 A_s + \frac{\omega_s^2(1+\chi^{(1)})}{c^2}A_s = -\omega_s^2\mu_0 P^{NL}(\omega_s)e^{-i(k_s z-\omega_s t)} \tag{3.8}$$

$$\nabla_T^2 A_a(z) - 2ik_a\frac{\partial A_a}{\partial z} + \frac{\partial^2 A_a}{\partial z^2} - k_a^2 A_a + \frac{\omega_a^2(1+\chi^{(1)})}{c^2}A_a = -\omega_a^2\mu_0 P^{NL}(\omega_a)e^{-i(-k_a z-\omega_a t)} \tag{3.9}$$

Now putting $1 + \mathrm{Re}(\chi) = n_0^2$ where n_0 is the linear refractive index, and using the relation $\frac{\omega^2 n_0^2}{c^2} = k^2$, we have

$$\nabla_T^2 A_p(z) + 2ik_p\frac{\partial A_p}{\partial z} + \frac{\partial^2 A_p}{\partial z^2} + \frac{i\omega_p^2}{c^2}\mathrm{Im}(\chi^{(1)})A_m = -\omega_m^2\mu_0 P^{NL}(\omega_p)e^{-i(k_p z-\omega_p t)} \tag{3.10}$$

$$\nabla_T^2 A_c(z) - 2ik_c\frac{\partial A_c}{\partial z} + \frac{\partial^2 A_c}{\partial z^2} + \frac{i\omega_c^2}{c^2}\mathrm{Im}(\chi^{(1)})A_c = -\omega_c^2\mu_0 P^{NL}(\omega_c)e^{-i(-k_c z-\omega_c t)} \tag{3.11}$$

$$\nabla_T^2 A_s(z) + 2ik_s\frac{\partial A_s}{\partial z} + \frac{\partial^2 A_s}{\partial z^2} + \frac{i\omega_s^2}{c^2}\mathrm{Im}(\chi^{(1)})A_s = -\omega_s^2\mu_0 P^{NL}(\omega_s)e^{-i(k_s z-\omega_s t)} \tag{3.12}$$

$$\nabla_T^2 A_a(z) - 2ik_a\frac{\partial A_a}{\partial z} + \frac{\partial^2 A_a}{\partial z^2} + \frac{i\omega_a^2}{c^2}\mathrm{Im}(\chi^{(1)})A_a = -\omega_a^2\mu_0 P^{NL}(\omega_a)e^{-i(-k_a z-\omega_a t)} \tag{3.13}$$

Using Slowly Varying Envelope Approximation,i.e.

$$\left|\frac{\partial^2 A}{\partial z^2}\right| \ll \left|k\frac{\partial A}{\partial z}\right| \tag{3.14}$$

Eq.3.10–Eq.3.13 can be written as

$$\nabla_T^2 A_p(z) + 2ik_p\frac{\partial A_p}{\partial z} + \frac{i\omega_p^2}{c^2}\mathrm{Im}(\chi^{(1)})A_m = -\omega_m^2\mu_0 P^{NL}(\omega_p)e^{-i(k_p z-\omega_p t)} \tag{3.15}$$

$$\nabla_T^2 A_c(z) - 2ik_c\frac{\partial A_c}{\partial z} + \frac{i\omega_c^2}{c^2}\mathrm{Im}(\chi^{(1)})A_c = -\omega_c^2\mu_0 P^{NL}(\omega_c)e^{-i(-k_c z-\omega_c t)} \tag{3.16}$$

$$\nabla_T^2 A_s(z) + 2ik_s\frac{\partial A_s}{\partial z} + \frac{i\omega_s^2}{c^2}\mathrm{Im}(\chi^{(1)})A_s = -\omega_s^2\mu_0 P^{NL}(\omega_s)e^{-i(k_s z-\omega_s t)} \tag{3.17}$$

$$\nabla_T^2 A_a(z) - 2ik_a\frac{\partial A_a}{\partial z} + \frac{i\omega_a^2}{c^2}\mathrm{Im}(\chi^{(1)})A_a = -\omega_a^2\mu_0 P^{NL}(\omega_a)e^{-i(-k_a z-\omega_a t)} \tag{3.18}$$

3.2.1 Non-Linear Polarizations

We will consider the four-wave mixing term for all the beams. self-phase modulation and cross-phase modulation effects are considered for Stokes and anti-Stokes beam along with FWM. We assume that the Stokes beam is cross-phase modulated by the pump beam whereas the anti-Stokes beam is cross-phase modulated by the control beam.

The non-linear polarization corresponding to the Stokes beam is given by

$$\begin{aligned} P^{NL}(\omega_s) =& \frac{3\epsilon_0}{4}\left[\chi^{(3)}_{spm}(\omega_s)|A_s|^2 + 2\chi^{(3)}_{xpm}(\omega_s)|A_p|^2\right]A_s e^{i(k_s z-\omega_s t)} \\ &+ \frac{3\epsilon_0}{2}\chi^{(3)}_{fwm}(\omega_s)A_p A_c A_a^* e^{i(k_p-k_c+k_a)z-i(\omega_p+\omega_c-\omega_a)t} \end{aligned} \tag{3.19}$$

The non-linear polarization corresponding to the anti-Stokes beam is given by

$$\begin{aligned} P^{NL}(\omega_a) =& \frac{3\epsilon_0}{4}\left[\chi^{(3)}_{spm}(\omega_a)|A_a|^2 + 2\chi^{(3)}_{xpm}(\omega_a)|A_c|^2\right]A_a e^{i(-k_a z-\omega_a t)} \\ &+ \frac{3\epsilon_0}{2}\chi^{(3)}_{fwm}(\omega_a)A_p A_c A_s^* e^{i(k_p-k_c-k_s)z-i(\omega_p+\omega_c-\omega_s)t} \end{aligned} \tag{3.20}$$

The non-linear polarization corresponding to the pump beam is given by

$$P^{NL}(\omega_p) = \frac{3\epsilon_0}{2}\chi^{(3)}_{fwm}(\omega_p)A_s A_a A_c^* e^{i(k_s-k_a+k_c)z-i(\omega_s+\omega_a-\omega_c)t} \tag{3.21}$$

The non-linear polarization corresponding to the control beam is given by

$$P^{NL}(\omega_c) = \frac{3\epsilon_0}{2}\chi^{(3)}_{fwm}(\omega_c)A_s A_a A_p^* e^{i(k_s-k_a-k_p)z-i(\omega_s+\omega_a-\omega_p)t} \tag{3.22}$$

3.2.2 Amplitude Equations for Generated fields

We assume that the pump and control fields are undepleted in the process. So, we will consider only the amplitude equations for the generated Stokes and anti-Stokes beams. Putting Eq.3.19 and Eq.3.20 into Eq.3.17 and Eq.3.18 respectively we get,

$$\begin{aligned}
&\nabla_T^2 A_s(z) + 2ik_s \frac{\partial A_s}{\partial z} \\
&= -\frac{i\omega_s^2}{c^2}\mathrm{Im}(\chi^{(1)})A_s - \frac{3\omega_s^2\mu_0\epsilon_0}{4}\left[\chi^{(3)}_{spm}(\omega_s)|A_s|^2 + 2\chi^{(3)}_{xpm}(\omega_s)|A_p|^2\right]A_s \\
&- \frac{3\omega_s^2\mu_0\epsilon_0}{2}\chi^{(3)}_{fwm}(\omega_s)A_pA_cA_a^*\exp[i(k_p - k_c + k_a - k_s)z - i(\omega_p + \omega_c - \omega_a + \omega_s)t]
\end{aligned} \tag{3.23}$$

$$\begin{aligned}
&\nabla_T^2 A_a(z) - 2ik_a \frac{\partial A_a}{\partial z} \\
&= -\frac{i\omega_a^2}{c^2}\mathrm{Im}(\chi^{(1)})A_a - \frac{3\omega_a^2\mu_0\epsilon_0}{4}\left[\chi^{(3)}_{spm}(\omega_a)|A_a|^2 + 2\chi^{(3)}_{xpm}(\omega_a)|A_c|^2\right]A_a \\
&- \frac{3\omega_a^2\mu_0\epsilon_0}{2}\chi^{(3)}_{fwm}(\omega_a)A_pA_cA_s^*\exp[i(k_p - k_c - k_s + k_a)z - i(\omega_p + \omega_c - \omega_s - \omega_a)t]
\end{aligned} \tag{3.24}$$

Initially, the self-phase modulation term is taken to be zero as the intensity of Stokes and anti-Stokes beams are quite small. But once they are generated we have to consider their effects. Conservation of energy tells that $\omega_p + \omega_c - \omega_s - \omega_a = 0$. We make the following substitutions to simplify the above equations (3.23) and (3.24).

$$\alpha_{s,a} = \frac{1}{2k_{s,a}}\left[\frac{\omega_{s,a}^2}{c^2}\mathrm{Im}(\chi^{(1)}) + \frac{3\omega_{s,a}^2}{2c^2}\mathrm{Im}\left(\chi^{(3)}_{\mathrm{xpm}}(\omega_{s,a})\right)|A_{p,c}|^2\right] \tag{3.25}$$

$$V_{s,a}(r) = \frac{3\omega_{s,a}^2}{2c^2}\mathrm{Re}\left(\chi^{(3)}_{\mathrm{xpm}}(\omega_{s,a})\right)|A_{p,c}|^2 \tag{3.26}$$

$$\kappa_{s,a} = \frac{3\omega_{s,a}^2\mu_0\epsilon_0}{4k_{s,a}}\chi^{(3)}_{\mathrm{fwm}}(\omega_{s,a})A_pA_c \tag{3.27}$$

$$\Delta k = k_p - k_c - k_s + k_a \tag{3.28}$$

Now we will discuss the physical significance of these terms. The coefficients $\alpha_{s,a}$ incorporate the imaginary component of the linear and nonlinear susceptibilities, $\mathrm{Im}[\chi^{(1)}]$ and $\mathrm{Im}[\chi^{(3)}]$, governing the gain (or absorption) of the Stokes (E_s) and anti-Stokes (E_a) fields within the medium. The term $V_{s,a}(r)A_{s,a}$ arises from the real

part of the third-order nonlinear susceptibility, $\mathrm{Re}[\chi^{(3)}]$, and manifests as an effective spatially varying potential - approximated as Gaussian - for the generated fields. This potential induces a position-dependent refractive index. The coupling coefficients $\kappa_{s,a}$ represent the strength of the FWM process, mediating energy exchange between the Stokes and anti-Stokes fields through the third-order nonlinearity. The wavevector mismatch Δ_k quantifies the deviation from perfect phase-matching.
Using the above substitutions, we can write the Amplitude equation for generated fields as

$$\boxed{\nabla_T^2 A_s + 2ik_s \frac{\partial A_s}{\partial z} = -2ik_s\alpha_s A_s - V_s(r)A_s - 2k_s\kappa_s A_a^* \exp(i\Delta kz)} \tag{3.29}$$

$$\boxed{\nabla_T^2 A_a - 2ik_a \frac{\partial A_a}{\partial z} = -2ik_a\alpha_a A_a - V_a(r)A_a - 2k_a\kappa_a A_s^* \exp(i\Delta kz)} \tag{3.30}$$

3.3 Outlook

So far, we have discussed the case where the pump and control beam are of a single frequency; then, the generated fields will have a single frequency. These systems are studied in [13, 17]. Now we end this chapter with certain open questions and try to address some of them in the next chapter.

As discussed earlier, the Stokes (E_s) and anti-Stokes (E_a) fields generate through spontaneous parametric generation and experience subsequent amplification via a non-degenerate four-wave mixing (FWM) process mediated by the third-order nonlinear susceptibility $\chi^{(3)}$ of the atomic medium. We ask the following questions, What will be the state before the Amplification process in MOPO? Can it go to the single photon level? What will be the bandwidth?

Now, we impose another question, which we will address in the next chapter. Suppose in this MOPO system, rather than providing a single-frequency pump field, we put multi-tone, i.e., a pump field consisting of multiple frequency components. Then, does the Stokes beam also show the multi-tone feature? Does the anti-Stokes field have the signature of multi-tone? What will be its bandwidth? We can ask a similar question: instead of providing multi-tone frequency, we now frequency modulate the pump field. How does this affect the signals of generated Stokes and anti-Stokes fields?

To study these phenomena, we have to prepare the frequency-modulated and multi-tone beam first. This is what we wish to discuss in the next chapter.

Chapter 4

Generating Multitone and Time-shared Beam using Acousto-Optic Modulator

As the name of the chapter suggests, the use of an Acousto-optic Modulator(AOM) is central to generate the "time-sharing" as well as multitone frequencies. The term "time-sharing" is taken from the nomenclature used in Optical tweezers. By "time-sharing", we mean multiple optical tweezers can be made from a single laser beam by sharing the time among them. In other words, we can trap multiple beads using the same laser beam by sharing the relaxation time of the bead among the trapping beads. So, it is clear that we need precise control over the laser beam so that we can move it as desired. There where the AOM/AOD comes into the picture. We are using AOM here because of its faster modulation. The basic principles of AOM is discussed in Section2.4. We will discuss in detail about these in this chapter.

4.1 Basic Alignment Procedures

We are using IPG Photonics YLR-40-1064-LP-SF laser. It is a continuous wave high-power fiber laser. It has a single frequency linearly polarised output. The wavelength is 1064 nm. The maximum power can go upto 40 watts. The atomic transitions of Rb requires 780 nm laser but here we are using 1064 nm laser to test the setup and see its effect. However, the setup including the AOM will also work for 780 nm laser. The camera Thorcam DCU224C is used for the detection part which is a CCD Camera with pixel size 4.65μm, square. Resolution is 1280×1024 pixels.

To align the beam, two mirrors and two identical apertures are used. The schematic of the setup is shown in Fig.4.1. One aperture is put closer to the Mirror 2, another aperture is placed very far away, towards the end of the optical table. Both the apertures are closed to minimum. By walking the beam, the beam is passed through both the apertures.

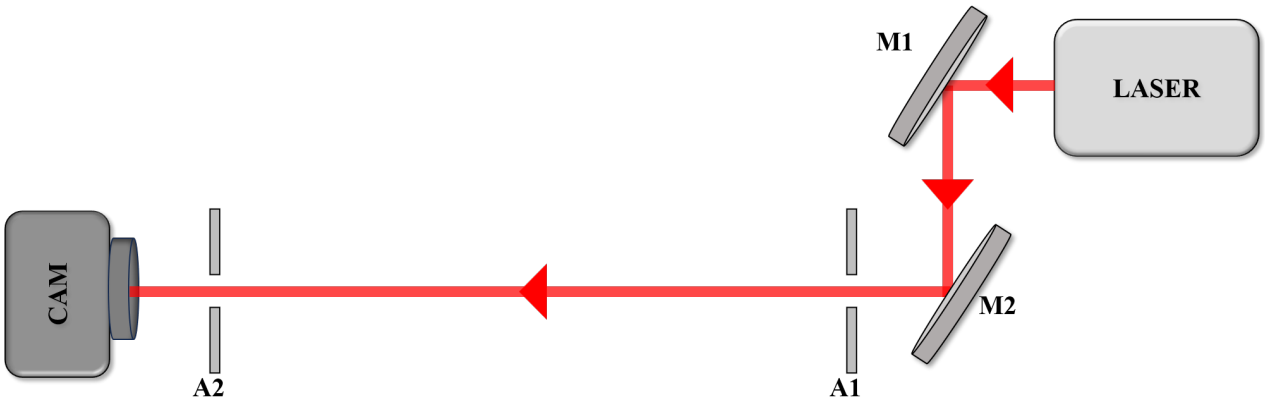

Figure 4.1: Alignment using two identical Apertures and two mirrors;
M: Mirror, A: Aperture

The key point to note here that the centre of symmetry of the beam should pass through the hole of the aperture. Then one expects a diffraction pattern of circular aperture in the camera which is called Airy pattern. We got the diffraction pattern Fig.4.2 in the camera, which is close to an Airy pattern. After getting the above diffraction pattern (Fig.4.2), we make sure that the beam is coming out symmetrically while opening the apertures. Two 20 cm lenses were put in the beam path. The focal length is chosen based on our choice of the following two AOM parameters: *Bragg angle* and the *response time*. The response time of the AOM is the time required by the acoustic wave to cross the optical beam diameter inside the crystal. The AOM *Gooch & Housego 3080-122* is used in our Experiment. It contains a TeO_2

crystal, and the velocity of the Acoustic wave inside the crystal is 4260 m/s. It has a central operating frequency (Acoustic wave) of 80 MHz and a bandwidth of 20 MHz. The Bragg angle of this AOM is 9.99 mrad, corresponding to the central frequency (Acoustic wave) at an optical frequency of 1064 nm. Hence, the separation between the 0^{th} order and 1^{st} order beam is 19.98 mrad.

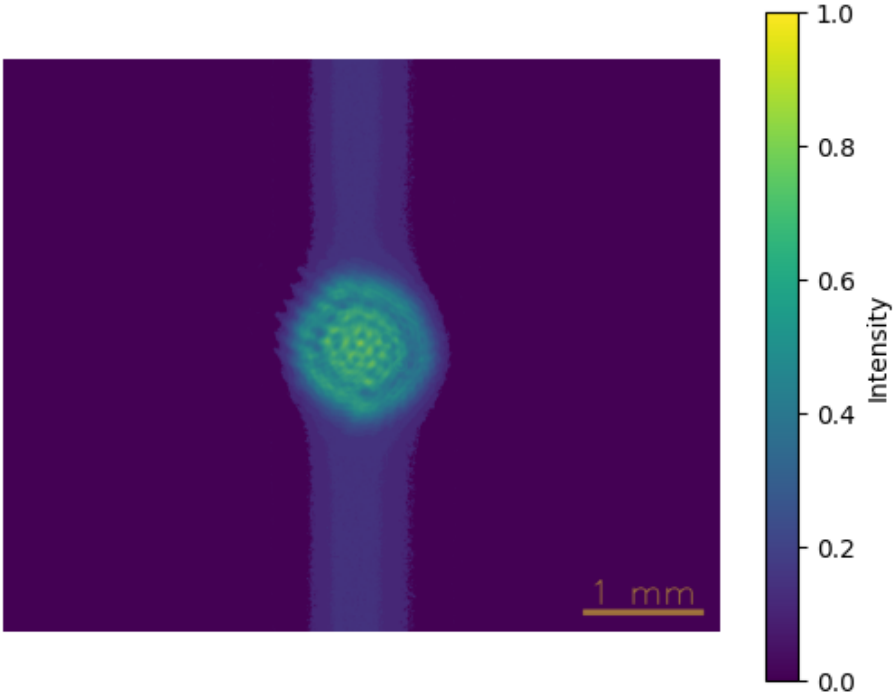

Figure 4.2: Fraunhofer diffraction pattern of the aperture obtained in the camera

Since our aim is to feed time-sharing and multitone frequency with the AOM, the response time of the AOM is of great importance to us. From the definition of the response time, it is clear that if we use a smaller beam size (i.e. lower focal length lens), then the response time will decrease. But, here comes another problem, the beam divergence at the focus will be larger compared to the Bragg angle. Then, the efficiency of the process will be greatly reduced. So, we have to ensure that the beam

divergence at the focus spot of the lens should be less (roughly, half or lower) than the Bragg angle. Table 4.1 shows the comparison of beam divergence vs spot size for different focal length lenses. The initial beam diameter is taken to be 2 mm for this calculation. Based on this calculation, we chose a 20 cm lens before the AOM (Table 4.1). Two 20 cm lenses were put in the confocal configuration in the beam path, i.e. the distance between the two lenses is 40 cm. The schematic setup is shown in Fig.4.3. We got the diffraction pattern similar to Fig.4.2 in the camera after aligning it. In such case of the confocal configuration of lenses, the first lens L1 focuses the beam and the second lens L2 collimates the beam. To check the collimation, we have taken the image of the beam at two different distances: one is near the lens and another very far from the lens. The Gaussian function is fitted to the horizontal profile of the beam, and the beam width is measured. Near the lens (5 cm away from the lens), the beam width ($1/e^2$ diameter) is found to be 1.6 mm, whereas at a very far distance (97.5 cm away from the lens), it is 2.4 mm. If we assume that the beam width is 1.6 mm just after collimation, then the natural divergence of the beam is given by, $\theta_0 = 4.23 \times 10^{-4}$ rad ($\theta_0 = \frac{\lambda}{\pi w_0}$, where w_0 is the $1/e^2$ radius). Now the angular change in the beam width while traveling a distance 92.5 cm is found to be $\theta = 4.56 \times 10^{-4}$ rad ($\theta = \frac{\text{Change in beam radius}}{\text{distance traveled}}$). Since the angular change is quite close to the natural divergence of the beam, we can infer that the beam is collimated.

The Acousto-Optic Modulator is placed at the focus of L1. Since the central frequency of the AOM is 80 MHz, the 80 MHz RF sine wave is provided by the Arbitrary Function generator (*Keysight 33622A*), via the Amplifier (*Mini-Circuits ZHL-1-2W+*) to the AOM. The AOM position is optimized for the maximum efficiency of the first-order beam for this particular lens combination. The beam separation angle between 0^{th} order and 1^{st} order beam is 19.98 mrad. The lens L2 collimates both beams and

Focal length of the lens (cm)	Beam diameter at the focus (μm)	Beam divergence (mrad)
5	25	19.98
10	50	9.99
15	75	6.66
20	100	4.99
25	124	3.99
30	149	3.33
35	174	2.85
40	198	2.50

Table 4.1: Beam diameter at the focus vs Beam divergence for different focal length lenses

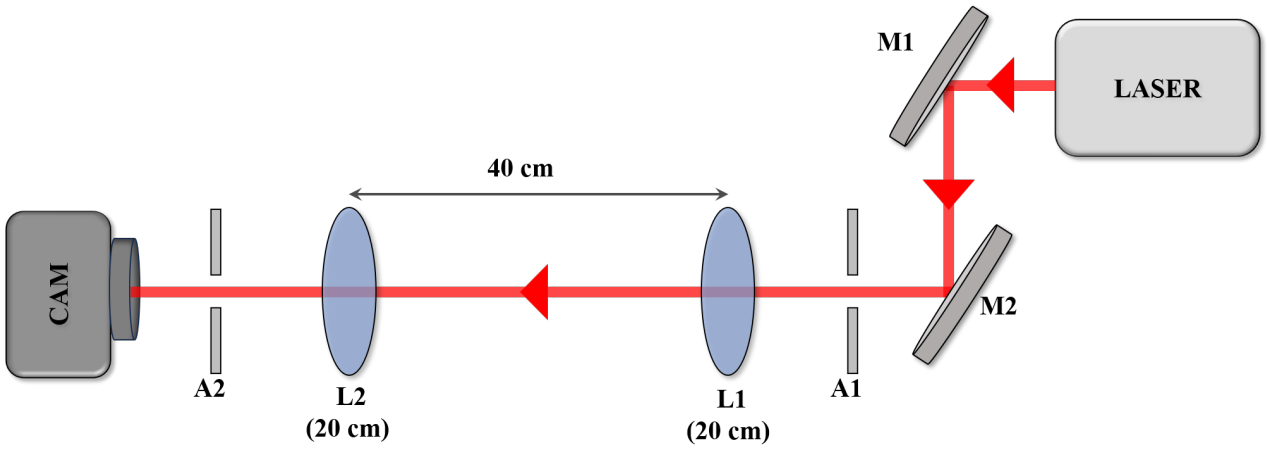

Figure 4.3: Alignment of two lenses in confocal configuration
M: Mirror, A: Aperture, L: Lens

makes them parallel with respect to each other. The aperture A2 is adjusted such that it will allow the 1^{st} order beam to pass through while blocking the 0^{th} order beam. Again to check the collimation of 1^{st} order beam, we again fitted the Gaussian function to the horizontal profile of the beam, but this time we found that the beam is not collimated. The reason behind it is the following: As mentioned, the AOM has TeO_2 crystal inside it. The refractive index of the TeO_2 crystal is 2.2079 at 1064 nm, and the length of the crystal is around 1 cm. Hence, the extra optical path length, $\Delta n \cdot L = (2.2079 - 1) \times 1 \approx 1.2$ cm. That means we have to put the second lens

1.2 cm closer to the AOM. So, we put the second lens L2 on a translation stage and adjusted accordingly to get the collimated beam.

The AOM is designed to operate in the Bragg regime, where we get only the first-order diffraction, and other higher-order diffractions have much lower efficiencies than the first-order. When light enters the AOM, it undergoes subsequent diffractions, and these diffraction orders undergo interference. The size of the crystal plays a very crucial role in determining which diffraction order undergoes constructive interference and which undergoes destructive interference. In our case, only the first-order survives, and to some extent, the second-order but with much lower intensity than the first-order. So, the diffraction effectively originates somewhere in between the front face and the midway between the crystal. So, we need to focus the beam precisely on the point where the diffraction starts. For this reason, another translation stage is used.The Schematic of the experimental setup is shown in Fig.4.4.

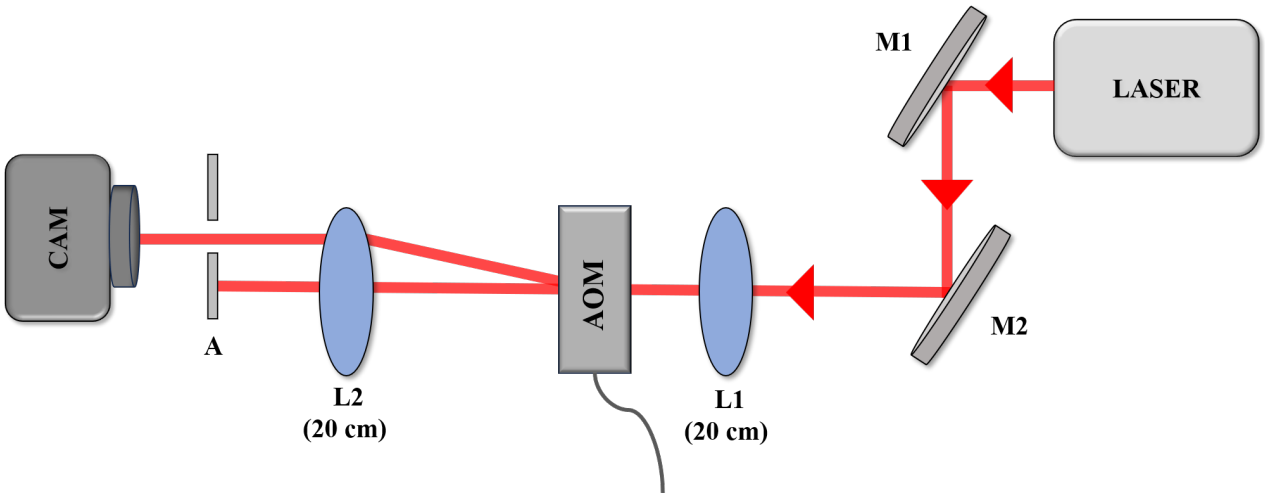

Figure 4.4: Initial Experimental setup for AOM
M: Mirror, A: Aperture, L: Lens

4.2 Observation and Analysis

When we change the frequency of the input RF, the beam separation angle between 0^{th} and 1^{st} order beam will change according to the formula,

$$\theta_{\mathrm{BS}} = \frac{\lambda F}{v} \tag{4.1}$$

where θ_{BS} denotes the beam separation angle, λ is the wavelength of the optical beam, F is the RF frequency, and v is the velocity of the acoustic wave inside the crystal. When we have provided 80 MHz RF input to the AOM, the angular separation between 0^{th} and 1^{st} order beam is obtained as 19.98 mrad. Now, if we provide two RF inputs that are 10 MHz apart, the relative angle between the 1^{st} order beams will be 2.49 mrad. An objective lens (*Thorlabs LMH-20X-1064*) is used in the beam path to focus the first-order beam of different frequencies to different points in the working distance of the objective. The working distance of the objective is 6 mm. Hence, the expected spatial shift in the working distance of the objective for RF frequencies that are 10 MHz apart is $(2.49 \times 10^{-3}) \times (6 \times 10^{-3}) = 14.94\ \mu m$. This distance is slightly more than 3 pixels. So, we expect to see two visibly distinct focus spots which are 10 MHz apart. Hence, we removed the lens, which is right after the AOM, and placed the objective lens there. A 4-f Imaging setup is made to image the working distance of the objective. An overview of the 4-f imaging setup is discussed in Chapter 2. Images are taken using a camera for three different frequencies (70 MHz, 80 MHz, and 90 MHz) within the bandwidth, each separated by 10 MHz. The centroid was fitted to each image, and the results are shown in Fig.4.5The background in Fig.4.5 represents the heatmap of the first-order beam corresponding to 80 MHz RF input. The x and y axes represents horizontal and vertical pixel number respectively. The centroid coordinates (in pixels) are $(300.95, 527.29)$, $(301.61, 527.22)$ and $(302.25, 527.09)$ for 70 MHz, 80 MHz and 90 MHz respectively. The horizontal shift from 70 MHz to 80

MHz is found to be 3.06μm, and from 80 MHz to 90 MHz is 2.97μm. Clearly, these are subpixel-level changes, and the measured values are significantly smaller than the analytically calculated shift (14.94 μm). We are measuring here the horizontal shift as the AOM is deflecting the first order beam along the horizontal direction as we change the input RF frequency. Then, we should not expect a change in the vertical distance, but a small change (0.32μm) in the same is observed which can be attributed to the error in the data analysis or our data acquisition system may not be ideal.

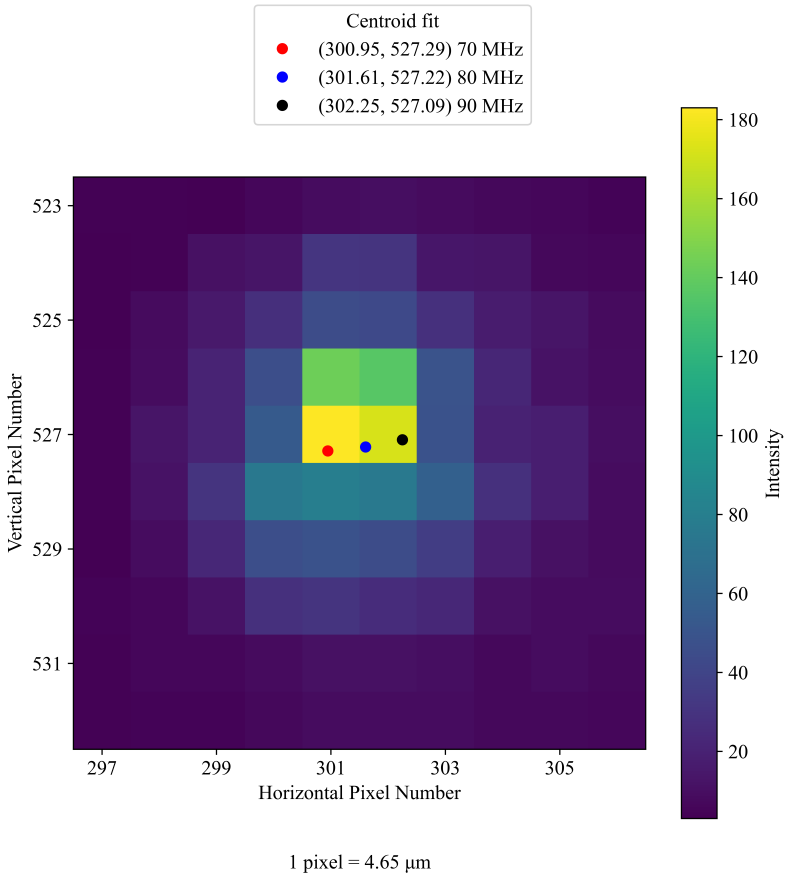

Figure 4.5: Heatmap of 80 MHz alongwith Centroid Calculation of 70 MHz, 80 MHz and 90 MHz

4.3 Generation and Detection of Multitone

In the context of the present chapter, by multitone, we mean the presence of multiple frequency components. The role of an arbitrary function generator is crucial in generating the multitone; this is the reason why we used it to provide the RF input to the AOM instead of conventional AOM Drivers. In order to program the arbitrary function generator, we keep the following parameters of the arbitrary function generator in mind. The sampling rate and the waveform length. The sampling rate is the number of samples that can be taken by the Digital to Analog converter in a given time interval. The Waveform length is the number of samples we feed to the arbitrary function generator. The *Keysight 33622A* model has a sampling rate of 1 μSa/s to 1 GSa/s, and the waveform length is 32 Sa to 4 Msa per channel. For our programming, we choose the sampling rate to be 1 Ga/s, the time interval to be 1 μs, and therefore, the number of samples is 1000.

4.3.1 Preliminary Observation of Multitone

The arbitrary function generator is programmed to provide the multitone containing 80 MHz and 90 MHz sinusoidal frequency components with equal amplitude and phase. The output data (first order beam) of the AOM is taken in the camera for three different input conditions: one with 80 MHz RF input, one with 90 MHz RF input, and one with the multitone input of 80 MHz and 90 MHz. The heatmap of all three output data is shown in Fig.4.6. We also plotted the horizontal intensity profile of all of them and fitted them with a Gaussian function in Fig.4.7.

The $1/e^2$ beam diameter of the output beams is measured from the Gaussian fit. The beam diameter is 2.1 mm for 80 MHz, 1.85 mm for 90 MHz and for the multitone is 2.43 mm. From Fig.4.7, we can observe that the multitone profile is an overlapping

combination of the 80 MHz and 90 MHz profiles. However, our goal is to achieve two distinct profiles simultaneously for the multitone, and therefore, it necessitates the need to improve the experimental setup itself.

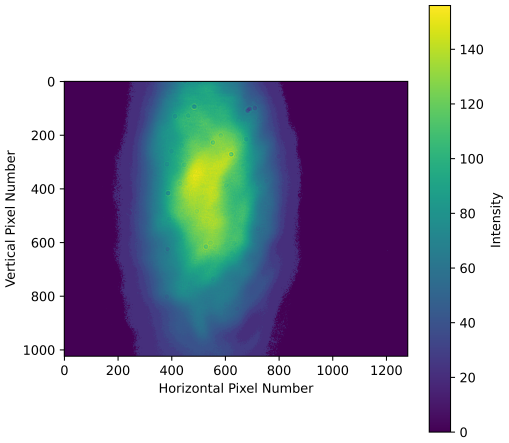

(a) Heatmap of First Order Beam at 80 MHz

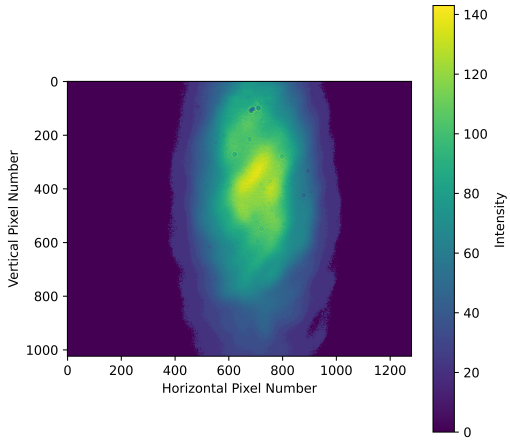

(b) Heatmap of First Order Beam at 90 MHz

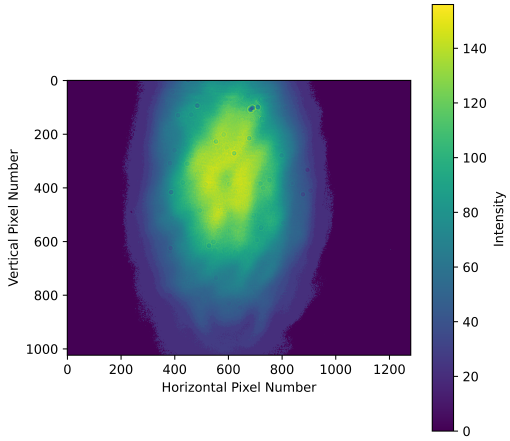

(c) Heatmap of First Order Beam at Multitone of 80 & 90 MHz

Figure 4.6: Comparison of Heatmap of Multitone with Individual Frequency Components

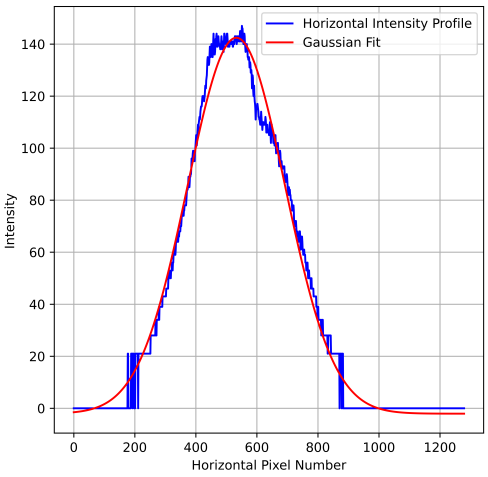

(a) 80 MHz

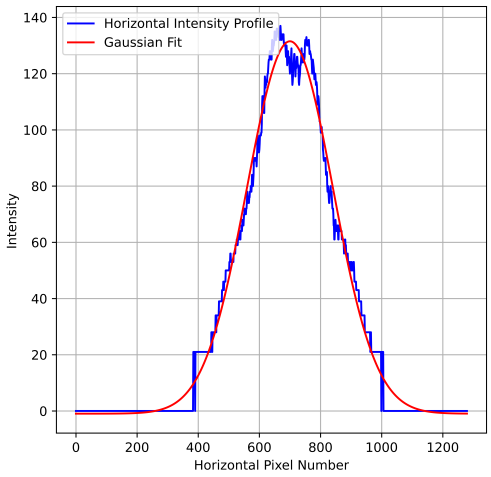

(b) 90 MHz

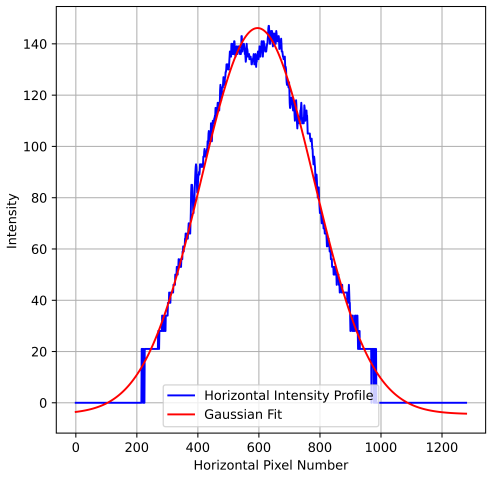

(c) Multitone of 80 & 90 MHz

Figure 4.7: Horizontal Intensity Profile of First Order Beams along with Gaussian Fit

4.3.2 Multitone and Time-shared Beam Analysis

We figure out the problem in our previous experimental setup. The lens before the AOM focuses the beam into the AOM, and since we put the Objective lens just after the AOM, we are getting the diverged beam in the Objective. Therefore, the angular change between the outputs of the AOM (first order) corresponding to different RF inputs is suppressed. To resolve this problem, the lens before the AOM is removed. The final experimental setup is shown in Fig.4.8.

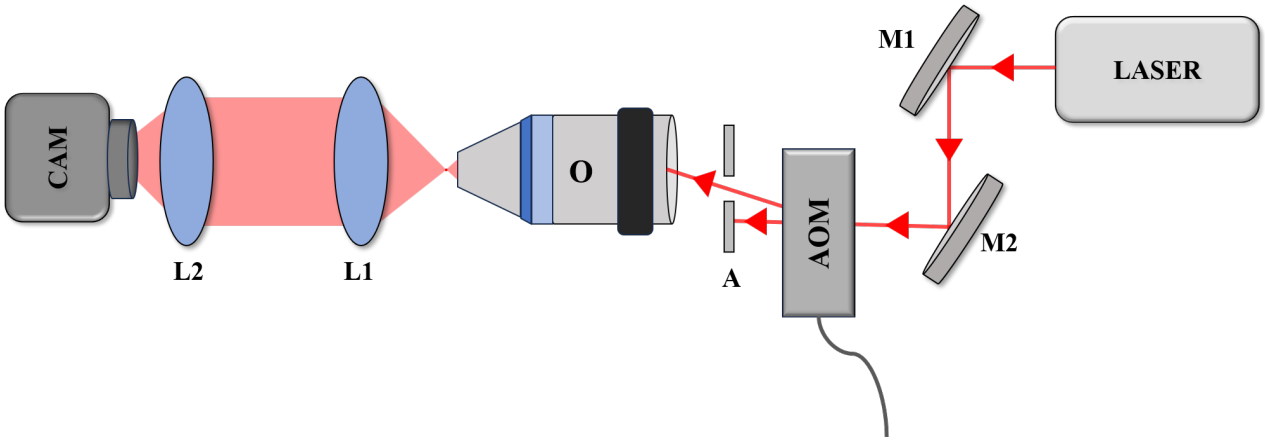

Figure 4.8: Experimental Setup

The multitone RF input containing 80 MHz and 90 MHz frequency components is provided to the AOM, and the first-order output is recorded in the camera. The heat map of the data, along with centroids, is shown in Fig.4.9.

The x and y-axis represent the absolute Horizontal and Vertical pixel numbers, respectively. The intensity scale is shown towards the left. The figure features two distinct high-intensity regions. Apart from that, there is a background noise predominantly observed in the lower part of the figure. A likely source of this noise can be attributed to the removal of the lens which was placed before the AOM. Now, the beam size being slightly greater than the AOM aperture, the scattering of the beam from the lower edge of the AOM aperture, contributes to the observed background noise. The

centroid is fitted to the two high-intensity regions individually. The red marker shows the centroid corresponding to the 80 MHz RF input, whereas the blue marker shows the centroid corresponding to the 90 MHz RF input. The centroid coordinates are $(295.66, 521.57)$ and $(299.52, 521.58)$ respectively. For the camera we used, the pixel size is 4.65 μm. The centroid shows a horizontal shift of 17.95 μm corresponding to the input frequencies, which are 10 MHz apart. This result is comparable to our analytical result (14.94 μm).

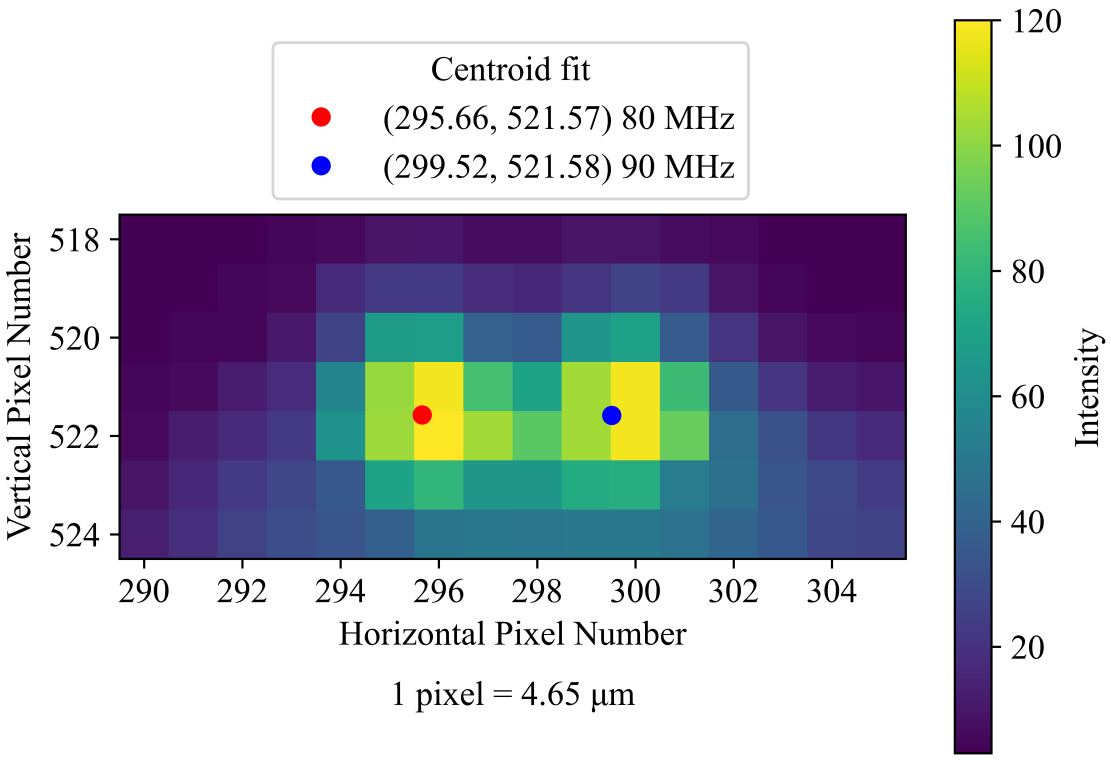

Figure 4.9: Heatmap of Multitone (80 MHz and 90 MHz) along with Cenroid fit

We followed the same analysis for the multitone with 64 MHz, 74 MHz, and 84 MHz frequency components. The heat map of the data, along with the centroids,

is shown in Fig.4.10. This figure features 3 distinct high-intensity regions. The red marker shows the centroid corresponding to the 64 MHz RF input, the blue marker corresponding to the 74 MHz RF input, whereas the black marker shows the centroid corresponding to the 84 MHz RF input. The intensity corresponding to 64 MHz is lower than the other two as it is outside the AOM bandwidth. The centroid coordinates are $(257.62, 533.71)$, $(262.63, 533.66)$ and $(267.56, 533.66)$ corresponding to 64 MHz, 74 MHz and 84 MHz respectively. The horizontal shift between the centroid of 64 MHz and 74 MHz is 23.3 μm, and between the centroid of 74 MHz and 84 MHz is 22.92 μm.

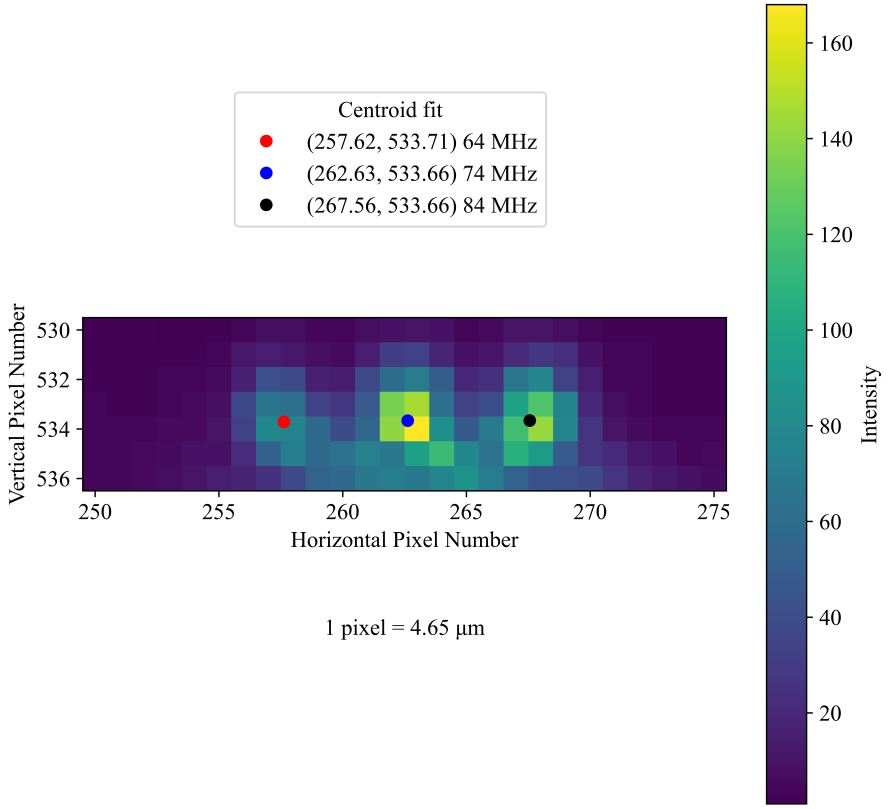

Figure 4.10: Heatmap of Multitone (64 MHz, 74 MHz, and 84 MHz) along with Cenroid fit

4.3.3 Time-shared Beam Analysis

Like the multitone generation, the role of the Arbitrary function generator is also very crucial for generating the time-sharing frequencies as well. The input RF is frequency-modulated to generate the time-shared beam. The frequency is centered at 74 MHz, with a frequency deviation of 10 MHz, and the modulation is driven by a sinusoidal signal with a frequency of 250 Hz. The modulation frequency is chosen by keeping in mind the exposure time of the camera. The modulation frequency has

to be larger than the inverse of the exposure time; to observe a 'static' image in the camera corresponding to all the frequencies from 64 MHz to 84 MHz. The heatmap of the data is shown in Fig.4.11. The x and y-axis represent the absolute Horizontal and Vertical pixel numbers, respectively. The intensity scale is shown towards the left. The figure shows an extended high-intensity region. The region roughly ranges from 269$^{\text{th}}$ pixel to 279$^{\text{th}}$ pixel, i.e., the length is 10 pixels, which corresponds to 46.5 μm. The horizontal shift between 64 MHz and 84 MHz, which we calculated from multitone analysis, is 46.22 μm.

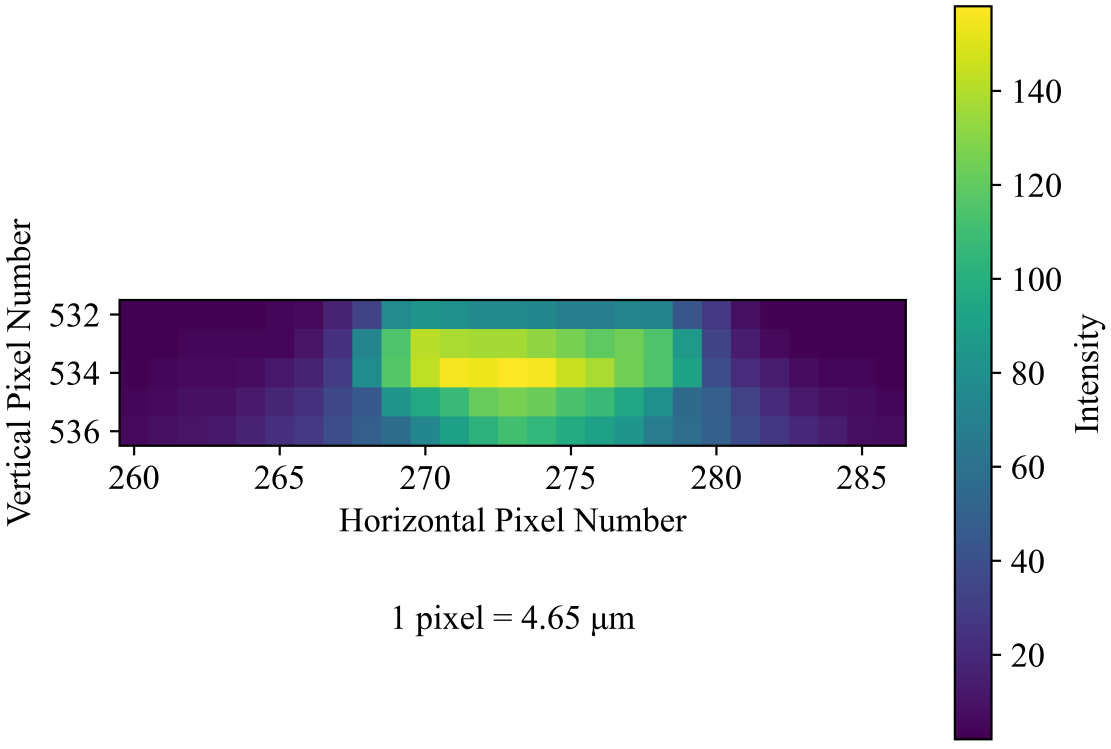

Figure 4.11: Heatmap Showing Time-shared Beam from 64 MHz to 84 MHz

Chapter 5

Conclusion and Outlook

This thesis, "Spectral and Spatial Modulation of Optical Pump Beam for Mirrorless Optical Parametric Oscillation," has explored the manipulation of pump beams used in MOPO through spectral and spatial modulation. The study utilized an AOM to generate multitone and time-shared pump beams, which can be used in the MOPO process to address key questions about their impact on the spectral and spatial properties of the resulting Stokes and anti-Stokes fields. Experimental results confirmed the generation of multitone beams with distinct frequency components (e.g., 80 MHz and 90 MHz, & 64 MHz, 74 MHz, and 84 MHz) and a time-shared beam spanning 64 MHz to 84 MHz, validated through 4-f imaging and centroid analysis. These findings highlight the potential of modulating pump beam characteristics to control the output fields' bandwidth and spatial distribution, advancing MOPO's practical utility. Looking ahead, this work opens several avenues for further exploration. The observed multitone and time-shared beam generation prompts investigation into their effects on MOPO efficiency, bandwidth, and quantum properties, such as single-photon generation or entanglement.

References

[1] Sushree Subhadarshinee Sahoo. *Application of fwm and xpm induced by ground-state coherence in thermal atomic vapor*. Ph.d. thesis, School of Physical Sciences, NISER, Bhubaneswar, 2020.

[2] SE Harris. Proposed backward wave oscillation in the infrared. *Applied Physics Letters*, 9(3):114–116, 1966.

[3] Carlota Canalias and Valdas Pasiskevicius. Mirrorless optical parametric oscillator. *Nature Photonics*, 1(8):459–462, 2007.

[4] Gustav Strömqvist, Valdas Pasiskevicius, Carlota Canalias, and Carlos Montes. Coherent phase-modulation transfer in counterpropagating parametric down-conversion. *Physical Review A—Atomic, Molecular, and Optical Physics*, 84(2):023825, 2011.

[5] Gustav Strömqvist, Valdas Pasiskevicius, Carlota Canalias, Pierre Aschieri, Antonio Picozzi, and Carlos Montes. Temporal coherence in mirrorless optical parametric oscillators. *Journal of the Optical Society of America B*, 29(6):1194–1202, 2012.

[6] Charlotte Liljestrand, Andrius Zukauskas, Valdas Pasiskevicius, and Carlota Canalias. Highly efficient mirrorless optical parametric oscillator pumped by nanosecond pulses. *Optics Letters*, 42(13):2435–2438, 2017.

[7] Danielle A Braje, Vlatko Balić, Sunil Goda, GY Yin, and SE Harris. Frequency mixing using electromagnetically induced transparency in cold atoms. *Physical review letters*, 93(18):183601, 2004.

[8] Shengwang Du, Jianming Wen, and Morton H Rubin. Narrowband biphoton generation near atomic resonance. *Journal of the Optical Society of America B*, 25(12):C98–C108, 2008.

[9] Shengwang Du, Pavel Kolchin, Chinmay Belthangady, GY Yin, and Stephen E Harris. Subnatural linewidth biphotons with controllable temporal length. *Physical review letters*, 100(18):183603, 2008.

[10] Vlatko Balić, Danielle A Braje, Pavel Kolchin, GY Yin, and Stephen E Harris. Generation of paired photons with controllable waveforms. *Physical review letters*, 94(18):183601, 2005.

[11] Pavel Kolchin. Electromagnetically-induced-transparency-based paired photon generation. *Physical Review A—Atomic, Molecular, and Optical Physics*, 75(3):033814, 2007.

[12] Yefeng Mei, Xianxin Guo, Luwei Zhao, and Shengwang Du. Mirrorless optical parametric oscillation with tunable threshold in cold atoms. *Physical Review Letters*, 119(15):150406, 2017.

[13] Sushree S. Sahoo, Snigdha S. Pati, and Ashok K. Mohapatra. Mirrorless optical parametric oscillator inside an all-optical waveguide. *Phys. Rev. A*, 98:063838, Dec 2018.

[14] R_E Slusher, LW Hollberg, Bernard Yurke, JC Mertz, and JF Valley. Observation of squeezed states generated by four-wave mixing in an optical cavity. *Physical review letters*, 55(22):2409, 1985.

[15] JL Oudar and YR Shen. Nonlinear spectroscopy by multiresonant four-wave mixing. *Physical Review A*, 22(3):1141, 1980.

[16] M Schmitt, G Knopp, A Materny, and W Kiefer. Femtosecond time-resolved four-wave mixing spectroscopy in iodine vapour. *Chemical physics letters*, 280(3-4):339–347, 1997.

[17] Sushree S Sahoo, Satya S Nayak, Soumya R Mishra, and Ashok K Mohapatra. Dissipative phase transition in a mirrorless optical parametric oscillator. *Physical Review A*, 102(5):053724, 2020.